NASA TECHNICAL MEMORANDUM

NASA TM-73,249

NASA TM-73,249

A DUAL-LOOP MODEL OF THE HUMAN CONTROLLER IN SINGLE-AXIS TRACKING TASKS

Ronald A. Hess

Ames Research Center
Moffett Field, Calif. 94035

May 1977

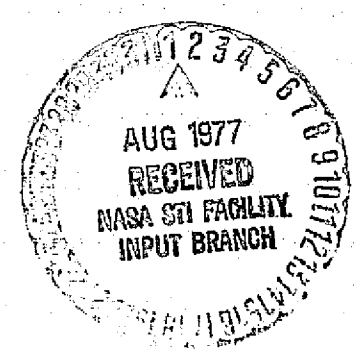

TABLE OF CONTENTS

SYMBOLS

a,b	integer exponents appearing in Y_{p_e} and $Y_{p_{\dot{m}}}$, respectively
c	command input
d	disturbance
e	$c - (m + d)$, error
e_d	$Y_d e$, displayed error
j	imaginary unit
K	controlled element gain
K_e	gain appearing in Y_{p_e}
$K_{\dot{m}}$	gain appearing in $Y_{p_{\dot{m}}}$
m	controlled element output
n_e	injected error remnant in single-loop human controller model
P_e	remnant model attention parameter
r_e	injected error remnant in outer-loop of dual-loop human controller model
$r_{\dot{u}}$	injected control rate remnant in inner-loop of dual-loop human controller model
s	Laplace variable
T_e	lag time constant appearing in Y_{p_e}, sec
T_L	lead time constant appearing in Y_{p_e}, sec
$T_{\dot{m}}$	washout time constant appearing in $Y_{p_{\dot{m}}}$, sec
u_c	$u_e - u_{\dot{m}}$, command to neuromuscular system
u_e	output of Y_{p_e}
$u_{\dot{m}}$	output of $Y_{p_{\dot{m}}}$
$\dot{u}_\delta$	force output of neuromuscular system
u_δ	rate of change of force output of neuromuscular system

w	disturbance
Y_c	controlled element dynamics
Y_d	display dynamics
Y_p	human controller single-loop describing function
Y_{p_e}	outer-loop equalization dynamics in dual-loop human controller model
Y_{p_m}	inner-loop equalization dynamics in dual-loop human controller model, sec
Y_{p_n}	human controller neuromuscular dynamics
Y_δ	manipulator dynamics
$Y_{\hat{\delta}}Y_c$	human controller's internal model of manipulator-controlled element dynamics
α_c	low-frequency phase droop parameter
δ	manipulator output
ζ_n	neuromuscular system damping ratio
$\zeta_{n_{CL}}$	damping ratio of closed-loop neuromuscular mode roots
λ	instability level in critical tracking tasks, rad/sec
λ_c	critical instability level in critical tracking tasks (value of λ at which control is lost), rad/sec
σ	real part of complex number
σ_x	root-mean-square value of variable x
τ	time delay, sec
τ_e	effective time delay, including phase effects of neuromuscular dynamics, sec
Φ_{xx}	power spectral density of variable x
Φ_{xx_a}	power spectral density of variable x_a
$\Phi_{xx_{ab}}$	cross power spectral density of variables x_a and x_b
ω	frequency, rad/sec

ω_c crossover frequency (frequency at which magnitude of open-loop transfer function equals unity), rad/sec

ω_n neuromuscular system undamped natural frequency, rad/sec

$\omega_{n_{CL}}$ undamped natural frequency of closed-loop neuromuscular mode roots, rad/sec

ω_p frequency of peak power, rad/sec

A DUAL-LOOP MODEL OF THE HUMAN CONTROLLER IN SINGLE-AXIS TRACKING TASKS

Ronald A. Hess

Ames Research Center

SUMMARY

A dual-loop model of the human controller in single-axis compensatory tracking tasks is introduced. This model possesses an inner-loop closure which involves feeding back that portion of controlled element output rate which is due to control activity. The sensory inputs to the human controller are assumed to be system error and control force. The former is assumed to be sensed via visual, aural, or tactile displays while the latter is assumed to be sensed in kinesthetic fashion. A nonlinear form of the model is briefly discussed. This model is then linearized and parameterized. A set of general adaptive characteristics for the parameterized model is hypothesized. These characteristics describe the manner in which the parameters in the linearized model will vary with such things as display quality. It is demonstrated that the parameterized model can produce controller describing functions which closely approximate those measured in laboratory tracking tasks for a wide variety of controlled elements. The explicit consideration of the inner-loop closure in the model allows much of the adaptive nature of the human controller to be explained in a systematic manner. In this respect, the dual-loop model is superior to existing single-loop structures. An empirically derived expression for the normalized injected error remnant spectrum is introduced. The expression utilizes a pair of the dual-loop model parameters. Finally, using the dual-loop model, the effects of some specific display and manipulator variations on controller describing functions, remnant spectra, and critical tracking task scores are explained.

INTRODUCTION

Single-Loop Model

Figure 1 is a simplified block diagram representation of a single-axis compensatory tracking task in which a human controller is attempting to maintain a controlled element at some specified equilibrium point. The controller views a display of system error (difference between actual and desired controlled element output) and uses a manipulator to generate input signals to the controlled element in order to drive the error to zero. Figure 2 shows the classical quasi-linear representation of human controller dynamics in the task of figure 1. Such quasi-linear models consisting of a describing function Y_p and a remnant signal n_e have provided the analytical basis for the vast majority of studies of systems under continuous manual

control. Measurements of Y_p and the power spectral density of n_e have been undertaken and reported for tasks involving a wide variety of controlled elements, disturbance characteristics, and manipulators (refs. 1 and 2).

To the author's knowledge, all the measurements of human controller dynamics in single-axis tasks have been predicated on the "single-loop" model of figure 2. This model has been employed because of its structural simplicity. The classical spectral techniques used in identifying controller dynamics are not capable of verifying more complex model structures under the restrictions implicit in figure 1, i.e., one disturbance and one manipulator (ref. 3).

Dual-Loop Model

It is the thesis of the research to be described that a more representative model of the actual signal processing structure of the human controller should exhibit an internal feedback loop which is not evident in the single-loop models now in common use. As will be seen, this hypothetical inner-loop involves a neuromuscular command signal derived from the rate of change of controlled element output which is due to human control activity. It is not the author's contention that the single-loop human controller models now in use are in any way incorrect, but rather that they contain an implicit but important internal loop closure which, if explicitly considered, can account for a good deal of the adaptive nature of the human controller in a systematic manner.

Figure 3 is a block diagram representation of the hypothetical human controller model alluded to in the previous paragraph. This model will be referred to as the "dual-loop" model of the human controller to distinguish it from the single-loop structure of figure 2. The dual-loop model was not derived from any physiological imperatives but rather stems from a structurally similar but philosophically different model discussed briefly by Smith in reference 4. In what follows, the dual-loop model will be linearized and then parameterized. A set of four general hypotheses describing the adaptive characteristics of the model will be set forth. While fulfilling the implicit and explicit constraints of these hypotheses, the model will be shown capable of systematically producing analytical single-loop describing functions which closely approximate those measured in laboratory tracking tasks. An empirically derived model for normalized injected error remnant spectra will be introduced. Finally, specific display/manipulator effects will be discussed and shown to be consistent with controller characteristics interpreted from the dual-loop structure.

DUAL-LOOP MODEL SPECIFICS

Linearization and Parameterization

The model of figure 3 is a nonlinear, possibly time-varying representation of the human controller in a single-axis compensatory tracking task. The sensory inputs to the human in this model are displayed error e_d and control force u_δ. The sensory modality for displayed error can be visual, aural, or tactile. Since u_δ is considered a control *force* applied by the human to the manipulator, u_δ is assumed to be sensed primarily by the Golgi tendon organs in the particular limb driving the manipulator (ref. 5).

The disturbance signal in figure 3 is shown injected into controlled element output for the sake of generality. In this way, the structure can represent a command input tracking task (d = -(command input)) or a disturbance regulation task (d = disturbance). If the actual disturbance is injected at some point other than the controlled element output, figure 3 is still valid; however, the spectral characteristics of d will reflect those of the actual disturbance and whatever dynamics precede the actual disturbance injection point. For example, if w is a disturbance injected into the manipulator output δ, the power spectral density of d in figure 3 would be given as

$$\Phi_{dd} = |Y_c|^2 \Phi_{ww} \tag{1}$$

While changes in input/disturbance spectral characteristics can be important, they have considerably less influence on human controller dynamics than the changes in controlled element dynamics, displays, and manipulators which will be encountered in this research. Hence, such input/disturbance effects will not be treated here.

The function of the inner loop in the model of figure 3 is to feedback equalized output rate u_m^* to the neuromuscular system. It is this feedback loop which immediately distinguishes the model from the single-loop structure of figure 2. The remaining neuromuscular command signal is equalized error u_e. The block labeled "thresholds and switching logic" is included to account for the possibility that the human can process only one of the sensory inputs u_δ or e_d at any instant. The selection of either of these inputs is assumed to be based upon nonlinear switching logic which, in turn, is a function of criterion or threshold values of u_δ and e_d. Any detailed discussion of the logic or threshold values is beyond the scope of this study which will essentially be concerned with the linearized form of figure 3 shown in figure 4.

As figure 4 indicates, the nonlinear thresholds and switching logic have been removed and a continuous, parallel processing structure has been utilized. Since the nature of the nonlinearities of figure 3 has only been hinted at here, any discussion of linearization is tentative at best. Suffice to say

that the nonlinearities are assumed to be amenable to quasi-linear representations in the inner and outer loops. Injected remnant signals r_e and $r_{\dot{u}}^*$, each with undetermined spectral characteristics are included to account for nonlinearities and/or time variations in quasi-linear fashion. The parameters associated with the linear model of figure 4 are presented in table 1. A brief discussion of each element of the quasi-linear human controller model follows.

Y_{p_e} — This equalization contains a simple first-order lead term and a high frequency lag term with break frequency $1/T_e$ which is beyond the undamped natural frequency ω_n of the neuromuscular system. For convenience, error rate utilization has been handled via a lead term in the error equalization. Alternatively, one could include a separate error-rate sensory input (if justified on physiological grounds) with equalization

$$Y_{p_{\dot{e}}} = K_e T_L/(T_e s + 1) \ .$$

The exponent a on the lag is included to implement more rapid fall-off in the filtering characteristics of Y_{p_e}, if necessary. It is hypothesized that the high bandwidth filter or lag represents the frequency limitations of the channel which processes displayed error. The values of the parameters K_e, T_L and to some extent T_e are assumed to be dependent upon controlled element dynamics, and display/manipulator characteristics.

$Y_{p_{\dot{m}}}$ — This equalization consists of a low frequency washout which, in terms of an acceptable feedback control system, is essential for inner-loop low frequency remnant suppression. Here "low frequency" refers to frequencies well below the open-loop crossover frequency ω_c. Inner-loop, low-frequency remnant power can arise from a variety of sources including errors in the low frequency portion of the controller's internal model of manipulator-controlled element dynamics $Y_{\delta}\hat{Y}_c$, poor kin-sthetic feedback u_{δ} at low frequencies or broadband process noise. As in any multiple-loop control system, noise (remnant) suppression will be much more essential in the inner-loop rather than in the outer-loop of the human controller model.

As shown in figure 4, the transfer function $u_{\delta}/r_{\dot{u}}$ can provide information regarding the closed-loop sensitivity of human controller output u_{δ} to inner-loop remnant $r_{\dot{u}}$. Specifically, the effect of inner-loop, low-frequency remnant will be minimized if

$$\left| \frac{u_{\delta}}{r_{\dot{u}}} (j\omega) \right|_{\omega<\omega_c} << 1.0 \qquad (2)$$

where $u_{\delta}/r_{\dot{u}}$ is given by

$$\frac{u_\delta}{r_{\dot{u}}} = \frac{-Y_{p_n} Y_{p_{\dot{m}}} \hat{Y_\delta Y_c}}{1 + Y_{p_n}(Y_d Y_{p_e} \hat{Y_\delta Y_c} + sY_{p_m} \hat{Y_\delta Y_c})} \tag{3}$$

It can be shown that a sufficient, and usually necessary, condition for the inequality of equation (2) to be satisfied is that $Y_{p_{\dot{m}}}$ possesses the washout characteristics shown in table 1.

Just as in the case of Y_{p_e}, the integer exponent b appearing in $Y_{p_{\dot{m}}}$ can be used to implement sharper washout characteristics, if necessary. Although Y_{p_e} contains a high frequency lag term to account for human controller bandwidth limitations in the outer loop, no such explicit limitation is incorporated in $Y_{p_{\dot{m}}}$ since it is assumed that the bandwidth limitations of the inner loop will be determined by the neuromuscular dynamics.

$\hat{Y_\delta Y_c}$— As table 1 indicates, $\hat{Y_\delta Y_c}$ represents the human controller's internal model of the manipulator-controlled element dynamics.

Y_{p_n} — This element represents the neuromuscular dynamics of the particular limb which drives the manipulator. The dynamics shown in table 1 have been deliberately simplified from the more elaborate neuromuscular model proposed in reference 5 for the sake of simplicity. With the inner loop of figure 4 closed, the quadratic form shown in table 1 can exhibit the salient features of the measured high frequency human controller dynamics, i.e., a typically subcritical damping ratio $\zeta_{n_{CL}}$, and a minimum second-order amplitude fall-off beyond the undamped natural frequency $\omega_{n_{CL}}$.

$r_e, r_{\dot{u}}$— The remnant signals r_e and $r_{\dot{u}}$ are injected into displayed error e_d and rate of change of control force $\dot{u}_\delta$. As mentioned previously, these remnant signals are part of a quasi-linear representation of the outer- and inner-loop human controller characteristics. The remnant $r_{\dot{u}}$ can also account for errors in the human controller's internal model of the manipulator-controlled element dynamics which would otherwise be neglected if $Y_\delta Y_c$ is used in place of $\hat{Y_\delta Y_c}$ in the inner loop of the model.

Adaptive Characteristics

Implicit in the dual-loop formulation is the assumption that the structure as outlined in table 1 is complete, i.e., no additions must be made or restructuring undertaken to account for human controller adaptation to various controlled elements, displays, manipulators, etc. The adaptive potential of the model is contained in the parameters of the inner- and outer-loop equalization and in the internal manipulator-controlled element model $\hat{Y_\delta Y_c}$. Indeed, the dominant adaptive feature of the dual-loop model is the explicit appearance of $\hat{Y_\delta Y_c}$ in the equivalent single-loop form of the model in table 1 (Y_p).

Four hypotheses regarding the general adaptive characteristics of the parameterized dual-loop human controller model are now offered:

Hypothesis 1. The parameters K_e, $K_{\dot{m}}$ and $T_{\dot{m}}$ act in consort with the internal model of the manipulator-controlled element dynamics $Y_{\hat{\delta}}Y_c$ to define the essential adaptive capabilities of the dual-loop model. The lead equalization in Y_{p_e} is used only when K_e, $K_{\dot{m}}$, $T_{\dot{m}}$, and $Y_{\hat{\delta}}Y_c$ themselves are unable to provide the effective lead equalization which may be required in a specific task.

Hypothesis 2. The relative utilization of the inner and outer loops of the dual-loop model is a function of manipulator-controlled element dynamics and the quality of the sensory inputs e_d and u_δ.

Hypothesis 3. Relative loop utilization in the dual-loop model can be quantified by the ratio $K_{\dot{m}}/K_e$.

Hypothesis 4. The value of $T_{\dot{m}}$ is determined by the extent to which the inner loop is utilized and by the quality of the internal model of the manipulator-controlled element dynamics $Y_{\hat{\delta}}Y_c$. The more the inner loop is utilized, the larger the value of $T_{\dot{m}}$. The more precise the internal model, the larger the value of $T_{\dot{m}}$.

No hypotheses regarding the adaptive nature of the parameters T_e ζ_n and ω_n are offered. These parameters effect primarily the high-frequency portion of the controller describing function Y_p ($\omega > 10$ rad/sec). Since measured data tends to be scant in this frequency range, verifying hypotheses regarding parameter variations would be difficult.

Describing Function Expressions

The last equation in table 1 is an expression for the equivalent single-loop human controller describing function Y_p in terms of the dual-loop entities Y_{p_e}, $Y_{p_{\dot{m}}}$, Y_{p_n} and $Y_{\hat{\delta}}Y_c$. By utilizing this equation and the remaining relations in table 1, the following describing function expressions can be obtained.

Small-bandwidth approximation— With $a = b = 1$ and with the simplifying approximations

$$\frac{K_e(T_L s + 1)}{T_e s + 1} \doteq K_e(T_L s + 1)$$

$$Y_{p_n} \doteq 1.0 \tag{4}$$

then,

$$Y_p = \frac{u_\delta}{e_d} = \frac{K_e(T_m^{\bullet}s + 1)(T_L s + 1)}{(K_m^{\bullet}Y_\delta \hat{Y}_c)s^2 + (T_m^{\bullet})s + 1} \tag{5}$$

Large-bandwidth approximation— With $a = b = 1$ and with the simplifying approximation

$$\frac{K_e(T_L s + 1)}{T_m^{\bullet}s + 1} = K_e(T_L s + 1)e^{-\tau s} \tag{6}$$

then,

$$Y_p = \frac{u_\delta}{e_d} = \frac{K_e(T_m^{\bullet}s + 1)(T_L s + 1)e^{-\tau s}}{(T_m^{\bullet}/\omega_n^2)s^3 + (2\zeta_n T_m^{\bullet}/\omega_n + K_m^{\bullet}Y_\delta \hat{Y}_c + 1/\omega_n^2)s^2 + (T_m^{\bullet} + 2\zeta_n/\omega_n)s + 1} \tag{7}$$

As will be seen, equations (5) and (7) and the general guidelines of the four hypotheses just stated, allow rapid "identification" of dual-loop model parameters using measured describing function data through the following two-step process. First, K_e, $K_m^{\bullet}$, $T_m^{\bullet}$, and, if necessary, T_L are selected using equation (5) and the low- to mid-frequency ($\omega \leq \omega_c$) describing function data. Second, ζ_n, ω_n and τ are chosen using equation (7), the selected values of K_e, $K_m^{\bullet}$, $T_m^{\bullet}$, and T_L, and the high-frequency ($\omega > \omega_c$) describing function data.

CONTROLLED ELEMENT EFFECTS

It will now be demonstrated that the dual-loop human controller model just outlined can produce describing functions which closely approximate those measured in laboratory tracking tasks. The following controlled element dynamics were used in the tasks under study: K, K/s, K/s^2, $K/(s^3 + 12.3s^2 + 11.6s)$, and $K/s(s - 1)$. An empirical remnant model will also be developed which approximates the measured remnant spectra for those experiments in which error injected remnant data were reported (all but the fourth task above). No formal numerical algorithm was utilized in identifying the dual-loop model parameters for the five experimental tasks. The parameter selection and adjustment procedure outlined previously was implemented by hand-fitting equations (5) and (7) to the describing function data. This informal approach was more than adequate for the purposes of this study. In addition, the difficulty of handling the implicit constraints of the four hypotheses regarding adaptive behavior precluded a more formal identification technique.

All of the manipulators used in the five experimental tasks to be studied were isometric (force) controllers. Thus, manipulator dynamics can be considered negligible as can display dynamics. With the obvious exception of

time derivatives and time related parameters, all elements of the closed-loop system of figure 4 are considered to be dimensionless entities. This is equivalent to relating the actual dimensions of all the elements (newtons, centimeters, etc.) to a pertinent nondimensional variable such as angle subtended at the human controller's eye by display indicator displacement (rad).

The measured describing functions for the K, K/s, and K/s^2 controlled element dynamics were taken from reference 6. The $K/(s^3 + 12.3s^2 + 11.6s)$ data were taken from reference 7, the $K/s(s - 1)$ data from reference 8.

$$Y_\delta Y_c = K \quad (K = 1.0)$$

Assuming $Y_{\hat{\delta}} Y_c = Y_\delta Y_c$, the following dual-loop model parameters were selected:

$K_e = 2.5$	$\zeta_n = 0.1$
$K_m^* = 0.5$ sec	$\omega_n = 20$ rad/sec
$T_L = 0$ sec	$\tau = 0.1$ sec
$T_m^* = 1.0$ sec	

With these parameters, equation (7) yields

$$Y_p = \frac{1 \cdot 10^3 (s + 1) e^{-0.1s}}{(s^2 + 1.98s + 1.97)(s + 203)} . \tag{8}$$

Figure 5 shows the measured and dual-loop model describing function comparison. The comparison is quite favorable, especially for frequencies beyond rad/sec. Note in particular that the dual loop describing function correctly indicates a low frequency lag being generated by the human despite the fact that no low-frequency lag term appears in the outer-loop error equalization Y_{p_e}.

$$Y_\delta Y_c = K/s \quad (K = 1.0)$$

Assuming $Y_{\hat{\delta}} Y_c = Y_\delta Y_c$, the following dual-loop model parameters were selected:

$K_e = 18.0$	$\zeta_n = 0.3$
$K_m^* = 6.0$ sec	$\omega_n = 15$ rad/sec
$T_L = 0$ sec	$\tau = 0.13$ sec
$T_m^* = 2.0$ rad/sec	

With these parameters, equation (7) yields

$$Y_p = \frac{4050.4(s + 0.5)e^{-0.13s}}{(s + 0.125)(s^2 + 9.38s + 903.5)} \tag{9}$$

The measured and dual-loop model describing function comparison is shown in figure 6. Of particular interest is the fact that the dual-loop model correctly reproduces the low-frequency phase droop of the experimental data.

$$Y_\delta Y_c = K/s^2 \qquad (K = 1.0)$$

Assuming $\hat{Y_\delta Y_c} = Y_\delta Y_c$, the following dual-loop model parameters were selected:

$K_e = 26.5$ $\qquad$ $\zeta_n = 0.7$

$K_m = 32.3$ sec $\qquad$ $\omega_n = 15$ rad/sec

$T_L = 0$ sec $\qquad$ $\tau = 0.16$ sec

$T_m = 3.33$ sec

With these parameters, equation (7) yields

$$Y_p = \frac{5960(s + 7.3)e^{-0.16s}}{(s^2 + 5.61s + 143.3)(s + 15.7)} \tag{10}$$

Figure 7 shows the measured and dual-loop describing function comparison. Note that although $T_L = 0$ sec, Y_p does indicate a low-frequency lead being generated.

$$Y_\delta Y_c = K/(s^3 + 12.3s^2 + 11.6s) \qquad (K = 145)$$

In using equation (5) with third-order dynamics, one is faced with factoring cubic polynomials in order to determine the poles of Y_p. This detracts from the utility of equation (5) for identification purposes. Hence, these third-order controlled element dynamics offer an opportunity for investigating the effect of an approximate lower-order internal model of the manipulator-controlled element dynamics. Figure 8 shows the exact controlled element transfer function and a second-order approximation valid beyond the crossover frequency. The low-frequency inaccuracies of the approximate internal model will be mitigated by the washout characteristics of Y_{p_m} and by the fact that the power in the feedback signal $\dot{u}_\delta$ is concentrated in the frequency region beyond crossover where the approximate model is reasonably accurate. By using the measured power spectrum for the control δ from reference 7, the spectrum for $\dot{u}_\delta$ was calculated and plotted in figure 8. Note that the peak at $\omega = \omega_p = 4.5$ rad/sec.

Using $Y_{\delta}\hat{Y}_c = 10/s^2$ from figure 8, the following dual-loop model parameters were selected:

$K_e = 1.4$ $\quad\quad$ $\zeta_n = 0.7$

$K_m^* = 1.0$ sec $\quad\quad$ $\omega_n = 15$ rad/sec

$T_L = 0$ sec $\quad\quad$ $\tau = 0.19$ sec

$T_m^* = 1.25$ sec

With these parameters, equation (7) yields

$$Y_p = \frac{312.7(s + 0.8)e^{-0.19s}}{(s^2 + 7.26s + 136.2)(s + 14.5)} \tag{11}$$

The measured and dual-loop model describing function comparison is shown in figure 9.

$$Y_{\delta}Y_c = K/s(s - 1) \qquad (K = 2.82)$$

In order to achieve an acceptable comparison between measured and dual-loop model describing functions for these dynamics, a higher order form of the dual-loop model had to be utilized. By referring to table 1 with $a = 1$, $b = 3$ and retaining the simplifying assumption of equation (6), a revised large bandwidth approximation for Y_p can be written as

$$Y_p = \frac{K_e(T_m^*s + 1)^3(T_Ls + 1)e^{-\tau s}}{d_5s^5 + d_4s^4 + d_3s^3 + d_2s^2 + d_1s + d_0} \tag{12}$$

where

$d_5 = T_m^{*3}/\omega_n^2$ $\quad\quad$ $d_2 = 1/\omega_n^2 + 6\zeta_n T_m^*/\omega_n + 3T_m^{*2}$

$d_4 = 3T_m^{*2}/\omega_n^2 + 2\zeta_n T_m^{*3}/\omega_n + K_m^* Y_{\delta}\hat{Y}_c$ $\quad\quad$ $d_1 = 2\zeta_n/\omega_n + 3T_m^*$

$d_3 = 3T_m^*/\omega_n^2 + 6\zeta_n T_m^{*2}/\omega_n + T_m^{*3}$ $\quad\quad$ $d_0 = 1.0$

Assuming $Y_{\delta}\hat{Y}_c = Y_{\delta}Y_c$, the following dual-loop model parameters were selected:

$K_e = 5.5$ $\quad\quad$ $\zeta_n = 0.1$

$K_m^* = 10.0$ sec $\quad\quad$ $\omega_n = 15$ rad/sec

$T_L = 0.33$ sec $\quad\quad$ $\tau = 0.15$ sec

$T_m^* = 3.33$ sec

With these parameters, equation (12) yields

$$Y_p = \frac{412.5(s + 0.3)^3(s - 1)(s + 3)e^{-0.15s}}{(s^2 + 0.329s + 0.0346)(s - 0.73)(s + 1.07)(s^2 + 2.24s + 223.2)} \tag{13}$$

Figure 10 shows the measured and dual-loop model describing function comparison. As the parameter list indicates, only a modicum of lead equalization in Y_{p_e} (actual error rate utilization) was required to match the experimental data.

Remnant Model

An expression for the equivalent, single-loop remnant n_e injected into the displayed error of the dual-loop model can be derived from figure 4 as

$$n_e = r_e - Y_\delta \hat{Y}_c \frac{Y_{p_{\dot{m}}}}{Y_{p_e}} r_{\dot{u}} \tag{14}$$

The power spectral density of n_e can then be given as

$$\Phi_{nn_e} = \Phi_{rr_e} + \left| Y_\delta \hat{Y}_c \frac{Y_{p_{\dot{m}}}}{Y_{p_e}} \right|^2 \left(\Phi_{rr_{\dot{u}}} - 2\Phi_{rr_{e\dot{u}}} \right) \tag{15}$$

where r_e and $r_{\dot{u}}$ have not been assumed to be statistically independent. As previously mentioned, no assumptions regarding the spectral characteristics of r_e and $r_{\dot{u}}$ are warranted without more detailed modeling of the nonlinear elements of figure 3. Since such a modeling effort is beyond the scope of this study, no further analytical remnant modeling will be discussed. However, an empirical expression for Φ_{nn_e} was developed which fits the measured injected remnant data satisfactorily. For the K, K/s, and K/s^2 dynamics, the normalized form of this expression is

$$\frac{\Phi_{nn_e}}{\sigma_e^2} = \frac{0.2(K_{\dot{m}}/K_e)}{1 + (K_{\dot{m}}/K_e)^2\omega^2/2} \tag{16}$$

For the $K/s(s - 1)$ dynamics, the numerator constant had to be modified to yield

$$\frac{\Phi_{nn_e}}{\sigma_e^2} = \frac{0.04(K_{\dot{m}}/K_e)}{1 + (K_{\dot{m}}/K_e)^2\omega^2/2} \tag{17}$$

Note that the models of equations (16) and (17) are dimensionally correct, i.e., both have dimensions of seconds.

Although the experimental remnant spectra for the K/s^2 and $K/s(s - 1)$ dynamics were based upon remnant injected into error *rate*, the author related these spectra to equivalent remnant injected into error via the relation (ref. 9)

$$\frac{\Phi_{nn_e}}{\sigma_e^2} = \frac{1}{\omega^2}\left(\frac{\Phi_{nn_{\dot{e}}}}{\sigma_{\dot{e}}^2}\right)\frac{\sigma_{\dot{e}}^2}{\sigma_e^2} \tag{18}$$

Values for $\Phi_{nn_{\dot{e}}}/\sigma_{\dot{e}}^2$ and $\sigma_{\dot{e}}^2/\sigma_e^2$ were obtained from the experimental data reported in references 6 and 8 for the K/s^2 and $K/s(s - 1)$ dynamics, respectively.

The fact that a different multiplying factor was necessary to fit the remnant data for the difficult-to-control $K/s(s - 1)$ dynamics suggests that this factor may be a function of human controller effort or attention level. Indeed, in modeling the human controller for the $K/s(s - 1)$ task, Levison *et al.* (ref. 8) had to accommodate the relatively small experimental remnant levels with smaller-than-usual model observation noise-signal ratios. They indicated that these smaller ratios were independent of controlled element characteristics and were the result of the controller attempting to improve root-mean-square tracking performance by reducing observation noise-signal ratios.

With the above in mind, a general remnant model was postulated with the leading multiplying factor (now denoted P_e) adjusted to account for human controller attention level.

$$\frac{\Phi_{nn_e}}{\sigma_e^2} = \frac{P_e(K_{\dot{m}}/K_e)}{1 + (K_{\dot{m}}/K_e)^2\omega^2/2} \tag{19}$$

$P_e = 0.2$ for "low" attention

$P_e = 0.04$ for "high" attention

Figures 11(a-d) compare the measured and empirical remnant spectra for the K, K/s, K/s^2, and $K/s(s - 1)$ dynamics. No injected remnant measurements were reported in reference 7 for the $K/(s^3 + 12.3s^2 + 11.6s)$ dynamics. Further experimental and empirical remnant correlations will be discussed in later sections.

Discussion

Table 2 summarizes the dual-loop modeling results. Figures 12 and 13 show the variation of K_m^*/K_e and $1/T_m^*$ for the five controlled elements discussed previously. Also included are modeling results for a peripheral viewing experiment ((denoted $K/s)_p$) to be described later. The controlled elements in figures 12 and 13 are ordered along the abscissa so that the corresponding K_m^*/K_e and $1/T_m^*$ values are monotonically increasing or decreasing, respectively. These figures represent graphical statements of the four adaptive hypotheses as applied to modeling efforts for the controlled elements shown.

Of particular interest is the fact that inner-loop utilization, as quantified by K_m^*/K_e, increases with controlled element difficulty. The relative positions of the elements K, K/s, K/s^2, and $K/s(s - 1)$ along the abscissa in figure 12, correspond to increasing "degrees of effort" as reported in reference 10 for tasks with these controlled element dynamics. If the value of T_m^* were hypothesized to be solely a function of relative loop utilization, then the order of controlled elements in figures 12 and 13 should be identical. This is not the case and hypothesis 4 clearly states so. Indeed, the relatively large value of $1/T_m^*$ for the $K/(s^3 + 12.3s^2 + 11.6s)$ dynamics is due to applying hypothesis 4 to a modeling effort which employed an approximate internal model for the manipulator-controlled element dynamics.

In summary, the analytical and experimental describing function and remnant spectra comparisons have indicated the following:

(1) Guided by the four hypotheses outlined previously, the dual-loop human controller model can produce describing functions which compare quite favorably with those from experiments for a wide variety of controlled elements.

(2) An empirical remnant model which utilizes two of the dual-loop model parameters can produce satisfactory comparisons with measured remnant spectra. Two distinct attention levels (P_e values) were necessary to satisfactorily match the data. Based upon what is known about human ability to allocate attention to a given task it is highly probable that a continuum of attention levels (P_e values) would be implied by a larger data base. Only two levels were used here for the sake of simplicity.

DISPLAY EFFECTS

It will now be demonstrated that the effects of two specific visual display characteristics are consistent with the adaptive structure of the dual-loop human controller model.

Peripheral Display

Levison *et al.* (ref. 8) conducted a study of compensatory tracking tasks, one of which involved separating the human controller's visual fixation point by 22° of visual arc from the error display. The controlled element consisted of the pure integrator dynamics (K/s, K = 1.0) discussed previously. Inspection of the measured human controller describing functions and injected remnant spectra reported in reference 8 reveals that for peripheral as opposed to foveal viewing, there appears to be

(1) an overall reduction in the amplitude ratio of the describing function,

(2) a reduction in the amount of low-frequency phase droop,

(3) an increase in the amount of high-frequency phase lag, and

(4) a reduction in the break frequency and a concomitant increase in the low-frequency amplitude of the injected remnant spectrum.

In terms of the dual-loop model, the principal impact of peripheral viewing is a decrease in the quality of the displayed error e_d as compared to that for foveal viewing. By assuming $Y_{\hat{\delta}}Y_c = Y_\delta Y_c$ and following the guidelines of the four adaptive hypotheses, the measured describing function data led to the selection of the following dual-loop model parameters for the peripheral viewing case:

$K_e = 5.6$ $\quad\quad$ $\zeta_n = 0.5$

$K_m^* = 10.0$ sec $\quad\quad$ $\omega_n = 20$ rad/sec

$T_L = 0$ sec $\quad\quad$ $\tau = 0.13$ sec

$T_m^* = 20.0$ sec

With these parameters, equation (7) yields

$$Y_p = \frac{2240(s + 0.05)e^{-0.13s}}{(s + 0.0333)(s^2 + 20s + 600)} \cdot \tag{20}$$

As figure 14 indicates, the dual-loop describing function and empirical remnant models match the measured data quite well. In particular, the low-attention remnant model does a fairly good job of matching the experimental remnant spectrum in spite of the fact that the former was empirically derived from *foveal* viewing data. Figures 12 and 13 show the magnitudes of K_m^*/K_e and $1/T_m^*$ for the peripheral viewing case, denoted $(K/s)_p$, and indicate increased inner-loop utilization when compared to the foveal viewing results with identical controlled element dynamics.

A comparison of figures 6, 11(b), and 14 indicates that the dual-loop describing functions and remnant spectra corroborate the somewhat subtle experimental differences between foveal and peripheral viewing just noted. With the exception of the third difference regarding increased phase lag with peripheral viewing, each of the variations can be attributed to the influence of a single dual-loop model parameter. The reduction in overall amplitude ratio is a result of the smaller K_e value for peripheral viewing. The reduction in high-frequency phase droop can be traced to the larger T_m^* value for the peripheral case. The reduction in the remnant break frequency and increase in low-frequency spectral amplitude can be attributed to the simultaneous increase in K_m^* and decrease in K_e for peripheral viewing.

The differences in the high-frequency phase lag between the foveal and peripheral viewing results are not immediately attributable to any single parameter in the dual-loop model. Note in table 1 that $\tau = 0.13$ sec for *both* viewing conditions. However, an examination of the root locus diagrams of the inner-loop closures for the two cases reveals that K_m^* and T_m^* play a dominant role in determining the positions of the closed-loop roots of the neuromuscular mode (those closed-loop roots emanating from the open-loop quadratic neuromuscular pair). The position of these closed-loop roots, in turn, influences the magnitude of the high-frequency phase lag in the describing function. Figures 15 and 16 show these root loci. Note that, for the foveal case (fig. 15), the roots of the neuromuscular mode have

$$\zeta_{n_{CL}} = 0.16, \qquad \omega_{n_{CL}} = 30 \text{ rad/sec}$$

while for the peripheral case (fig. 16), these roots have

$$\zeta_{n_{CL}} = 0.41, \qquad \omega_{n_{CL}} = 24.5 \text{ rad/sec} .$$

The larger damping ratio and smaller undamped natural frequency of the peripheral case cause an increase in high-frequency phase lag. Note also that the larger lag for the peripheral case is *not* attributable to the position of the open-loop neuromuscular quadratic pair.

Quantized Display

Differences in measured controller describing functions and remnant spectra have also been noted in other experimental tracking tasks studies involving degradation of display quality. Jex *et al.* (ref. 11) investigated the effects of error display quantization on human tracking performance, describing functions and remnant. By using controlled element dynamics of $K/s(s + 2)$, a quantized display was situated a nominal 57 cm from the controller's eyes. The display quanta level was 0.25 cm. In comparison to a continuous nonquantized display, the quantized display resulted in an average 22% decrease in human controller gain, an average 34% increase in "effective" time delay (which includes the effect of phase lags due to neuromuscular dynamics), and a 48% decrease in the low-frequency phase droop

parameter α_c, associated with the "extended crossover" human controller model (ref. 1). Since remnant power spectra were typically measured at only four frequencies, no conclusions regarding changes in remnant break frequency were possible, however, a definite increase in the low-frequency amplitude was noted with the quantized display.

The describing function effects reported in reference 11 for continuous vs quantized displays are very similar to those gleaned from reference 8 for foveal vs peripheral display conditions. Both sets of measured effects can be explained via the dual-loop model structure and its adaptive characteristics. In both cases, as the quality of the displayed-error decreases, the utilization of the inner-loop increases, with concomitant increases in K_m^*/K_e and T_m^*. These parameter changes then result in decreased describing function amplitude, decreased low-frequency phase droop, increased high frequency phase lag, and increased low-frequency remnant spectrum amplitude.

The similarity between peripheral display effects and quantized display effects allow an explanation of some interesting critical tracking task data reported by Hess and Teichgraber (ref. 12). In reference 12, a series of compensatory tracking tasks were described in which the error display was quantized. Unlike the work of reference 11, however, a total of 8 quantization levels were utilized ranging from 0 cm (continuous) to 1.69 cm as shown in figure 17. The display was mounted a nominal 50 cm from the controller's eyes. The critical tracking task was mechanized in single and dual-axis format (ref. 13), however, only the single-axis data is immediately pertinent.

The single-axis critical tracking task employed an unstable controlled element of the form

$$Y_c = \frac{K\lambda}{s^{n-1}(s - \lambda)} \tag{21}$$

where n is the task order. A "1.5" order controlled element was also defined

$$Y_c = \frac{K\lambda}{(s + 2)(s - \lambda)} \tag{22}$$

This provided an intermediate element between the first and second-order dynamics (n = 1,2). In terms of the single-loop model of the human controller, the three critical task controlled elements require no, some and full lead equalization by the human controller for the first-order, 1.5 order and second-order controlled elements, respectively (refs. 11,13). In all of these controlled elements, the degree of instability λ was slowly and monotonically increased from a small positive value until the operator could no longer maintain control. The value of λ at which control was lost was denoted λ_c and referred to as the "critical instability score." No input signal was required in the critical tracking tasks since operator remnant served to excite the system.

Single-axis critical instability scores are excellent indicators of the closed-loop system bandwidth and of the effective human-controller time delay in tracking (ref. 13). Decrements in λ_c resulting from substitution of a different form of display for an ideal display can be used as reliable indicators of the effective time delay penalties incurred by the nonideal displays.

Figures 18 and 19 illustrate the dependence of the single-axis critical instability score λ_c upon the quanta level for the three controlled elements using two test subjects denoted A and B. Each data point indicates the mean value of λ_c for 20 runs. Standard deviations were typically within a symbol width in magnitude and were not indicated in the figures. No data were taken for the higher-order systems and coarser quantization formants in which control could not be maintained for at least 10 sec. As figures 18 and 19 indicate, the increasing display quanta levels result in decreasing instability scores for the three controlled elements studied. These decreased instability scores can be equated to increased human controller effective time delays.

The most surprising result of the experiment from the standpoint of *single-loop* human controller models is the fact that the fitted straight lines in figures 18 and 19 are nearly parallel. The necessity of lead equalization has little, if any, effect on the gradient of critical task scores with respect to quanta level. This is surprising because

1. The amount of lead equalization must increase as the order of the critical task increases,

2. According to the generally accepted interpretation of the single-loop human controller model, lead equalization is accomplished through direct sensing of error rate or through differentiation of the error signal (ref. 14) and

3. Quantization degrades the human controller's ability to sense or derive actual error rate.

Thus, from items (1), (2), and (3), one would expect that those critical tasks requiring more lead equalization would be more adversely affected by quantization. Clearly, this is not corroborated by experiment.

If the critical task scores are interpreted in light of the dual-loop human controller model, however, the results are quite reasonable:

1. Decreased display quality can yield increased high frequency phase lag attributable to the effect of increased inner-loop gain K_m' and increased T_m' on the position of the closed-loop neuromuscular mode roots. This can explain the decreasing instability scores with increasing quanta levels for all the controlled elements.

2. The lead equalization apparent in measured single-loop describing functions can, for the most part, be explained by inner-loop activity in a

dual-loop model. This activity is *not* related to sensing error rate or deriving it from error displacement, and will *not* be inhibited by quantization. This can explain the nearly parallel straight lines in figures 18 and 19. The effects of the modicum of true outer-loop error rate utilization which may be involved in the second-order task (see table 2, $Y_\delta Y_c = K/s(s - 1)$) will be mitigated by increased inner-loop utilization due to task difficulty and display quality.

Discussion

It has been shown that the dual-loop model can explain the documented effects of two specific variations in display quality. Of particular interest was the manner in which changes in the high-frequency phase lag could be attributed to variations in K_m^* and T_m^* in the dual-loop model. Although these changes were associated with tasks having identical controlled element dynamics, similar results can be demonstrated for a pair of tasks involving different controlled elements. In particular, the documented increments in high frequency phase lag (or effective time delay) associated with tasks requiring increased amounts of controller lead equalization (in the single-loop sense) can be explained via the dual-loop model.

Figure 20 shows the root locus diagram for the inner-loop closure of the model for K/s^2 controlled element dynamics. Comparing the locations of the closed-loop neuromuscular mode roots for figure 20 and that for figure 15 for K/s dynamics, one sees the reason for the larger high-frequency phase lag in the former case. The lower value of $\omega_{n_{CL}}$ for the K/s^2 dynamics causes an increased phase lag to occur in the human controller model beyond crossover over and above the slight increase attributable to the increment in τ noted in table 2. In terms of the crossover human controller model which subsumes high frequency describing function characteristics into an effective time delay τ_e, the K/s^2 dynamics will appear to induce a larger τ_e than the K/s dynamics.

MANIPULATOR EFFECTS

In discussing the structure of the human controller model in figures 3 and 4, it was stated that controller output u_δ would be considered a control *force* for the purposes of kinesthetic feedback. Although joint position sensors and muscle spindles in the limb affecting control can sense absolute limb *position* (ref. 5), general manipulator characteristics probably favor force feedback in the human controller. This is because the null point in the output of a manipulator ($\delta = 0$) is normally coincident with the null point in human controller *force* output ($u_\delta = 0$), the latter being easily detectable by the human controller. The ability of the human to precisely correlate a specific limb *position* with the manipulator output null point, however, is considerably weaker (ref. 15).

The discussion which follows concerns the effects of depriving the human controller of force feedback by using a free or unrestrained manipulator. The performance of the human controller when using the free manipulator is compared to that using a pure force or isometric manipulator in a series of first and second-order critical tracking tasks as reported in reference 15. In terms of the dual-loop human controller model, the use of an unrestrained manipulator can result in a considerable degradation in the quality of the kinesthetic feedback u_δ. A gross assessment of the effects of this degradation can be obtained analytically by simply considering the qualitative aspects of opening the inner feedback loop in figures 3 and 4.

Force and Free Manipulator Restraints

McDonnell and Jex (ref. 15) investigated the effects of control stick stiffness on human controller performance in terms of first and second-order critical instability scores. The result which is of pertinence to this discussion was stated by the authors as follows:

> "Another unresolved observation regards the control stick. In the first-order case, the type of stick (force, spring or free) made little difference in behavior. For the second-order case, however, the operator was unable to control even the smallest instability with the free stick. His subjective impression was that lack of a null-control reference was the difficulty."

One plausible explanation of these effects can be offered by considering the particular dual-loop model parameters which yield satisfactory describing function and remnant spectra comparisons for first- and second-order subcritical tracking tasks (fixed level of instability λ).

$Y_\delta Y_c = K/(s - 2)$ $(K = 2.0)$— Reference 13 discusses describing function and remnant measurements for single-axis tasks which employed, among others, $K/(s - 2)$ controlled element dynamics. For the purposes of the discussion to follow, one adequate representation of the dual-loop human controller describing function can be obtained by including an effective time delay τ_e in the small-bandwidth approximation of equation (5). Thus,

$$Y_p = \frac{K_e(T_m^* s + 1)(T_L s + 1)e^{-\tau_e s}}{(K_m^* Y_\delta \hat{Y}_c)s^2 + (T_m^*)s + 1} \tag{23}$$

Assuming $Y_\delta \hat{Y}_c = Y_\delta Y_c$, the following dual-loop model parameters were selected

$K_e = 5.0$ $\qquad$ $T_m^* = 0.36$ sec

$K_m^* = 0.20$ sec $\qquad$ $\tau_e = 0.1$ sec

$T_L = 0$ sec

Figure 21 shows the measured and dual-loop model describing function and remnant comparison. The break frequency of the empirical remnant model is well beyond the highest frequency of the experimental measurements.

The inability of the selected parameters to produce a describing function which included the low-frequency phase droop evident in the experimental data of figure 21 plus the suspiciously low value of $K_m^\bullet/K_e$ for these controlled element dynamics ($K_m^\bullet/K_e = 0.04$ sec) led to a second model formulation. This second model used a simplified internal model for the $K/(s - 2)$ dynamics, namely K/s. Figure 22 shows the approximate and exact manipulator-controlled element transfer function characteristics. Just as in figure 8, the low-frequency comparison is quite poor, while the comparison for frequencies above crossover improves considerably. Revised dual-loop model parameters were selected as

$$K_e = 18.0 \qquad T_m^\bullet = 3.33 \text{ sec}$$

$$K_m^\bullet = 7.0 \text{ sec} \qquad \tau_e = 0.11 \text{ sec}$$

$$T_L = 0 \text{ sec}$$

With these parameters, equation (23) yields

$$Y_p = \frac{3.47(s + 0.3)e^{-0.11s}}{(s + 0.058)} \tag{24}$$

Figure 23 shows the measured and dual-loop model describing function and remnant comparison. The comparison is considerably better than that of figure 21. The ratio $K_m^\bullet/K_e$ is now 0.39 sec which, according to figure 12, places the controlled element between the K/s and $K/(s^3 + 12.3s^2 + 11.6s)$ dynamics.

Using the controller model of equation (24), the simplified internal model of figure 22 and the command input spectra used in the experiments of reference 13, the correlated control rate spectrum $\Phi_{\dot{u}u_\delta}$ was calculated and is shown in figure 24. The approximate and exact manipulator-controlled element transfer functions are also repeated from figure 23. Note that the power in the correlated control rate spectrum is greatest beyond the open-loop crossover frequency. Since the model used in obtaining equation (24) contained no neuromuscular dynamics, $\Phi_{\dot{u}\dot{u}_\delta}$ was not calculated beyond $\omega = 10$ rad/sec. From figure 24 it can be seen that the low-frequency inaccuracies of the approximate internal model are mitigated by the washout characteristics of $Y_{p_m^\bullet}$ and by the fact that the power in the feedback signal $\dot{u}_\delta$ is concentrated in the frequency region where the approximate model is reasonably accurate.

Now, the experimental evidence of reference 15 indicating the small degradation in human controller performance in first-order critical tasks with a free manipulator is qualitatively consistent with the dual-loop modeling

results. In terms of K_m^*/K_e, the inner-loop is not being utilized to a great extent. In this task, K_m^*/K_e = 0.39 sec, a value which is among the lowest of those shown in figure 12. Thus, the effects of a free manipulator (analytically generated by opening the inner loop) are mitigated considerably.

$Y_\delta Y_c = K/s^2$ $(K = 1.0)$— Since reference 15 states that even the smallest instability in the second-order critical task was uncontrollable with a free manipulator, a re-examination of dual-loop model parameters for the K/s^2 controlled element dynamics ($\lambda = 0$) is in order. The selected model parameters for the K/s^2 controlled element dynamics are repeated here for convenience.

$K_e = 26.5$ $\quad\quad$ $\zeta_n = 0.7$

$K_m^* = 32.3$ sec $\quad\quad$ $\omega_n = 15$ rad/sec

$T_L = 0$ sec $\quad\quad$ $\tau = 0.16$ sec

$T_m^* = 3.33$ sec

Now the experimental evidence of reference 15 indicating the uncontrollability of the second-order critical task with a free manipulator is qualitatively consistent with the dual-loop modeling results. In terms of K_m^*/K_e, the inner-loop is being utilized to a considerable extent with $\lambda = 0$. Here $K_m^*/K_e = 1.22$ sec which is over 3 times the value for the first-order critical task with $\lambda = 2$. Thus, the effects of a free manipulator (analytically generated by opening the inner-loop) are amplified as compared to the first-order task. In addition, the inner-loop is even more essential as λ increases from zero. Note that in figure 12, with $\lambda = 1$, $K_m^*/K_e = 1.82$ sec, which is 4.7 times the value for the first-order critical task with $\lambda = 2$.

Discussion

It has been shown that the effects of manipulator characteristics upon human controller performance in a pair of critical tracking tasks are qualitatively consistent with the dual-loop model structure. Previous modeling results have indicated that the inner-loop of the dual-loop model becomes increasingly important as task difficulty increases. This has been corroborated by experimental results which show that if manipulator characteristics provide poor kinesthetic feedback (with implied inhibition of inner-loop activity) measured human controller performance suffers in proportion to task difficulty.

The results of modeling the human controller with $K/(s - 2)$ controlled element dynamics, also give rise to the conjecture that the use of simplified internal models for manipulator-controlled element dynamics may not only be more tractable from an analytical standpoint, but also more appropriate from a structural standpoint.

CONCLUSIONS AND RECOMMENDATIONS

The assessment of a dual-loop model of the human controller which was undertaken in this study leads to the following conclusions:

1. The proposed dual-loop model and the general adaptive characteristics which have been hypothesized can produce human controller describing functions which closely approximate those measured in a wide variety of single-axis compensatory tracking tasks.

2. An empirical model for injected remnant spectra employing low- and high-controller-attention levels can approximate experimentally derived injected remnant spectra. Of the six experiments to which the remnant models were applied, the low-attention model satisfactorily matched the data for the four *stable* controlled elements while the high-attention model matched the data for the two *unstable* elements.

3. The dual-loop model and associated hypotheses can explain the measured variations in human controller dynamics and performance which accompany changes in controlled element dynamics and variations in display and manipulator characteristics.

4. In terms of existing single-loop models, the dual-loop model exhibits the following novel features:

(a) The adaptive nature of the model is due primarily to the existence of an explicit internal model of the manipulator-controlled element dynamics in an inner feedback loop.

(b) In controlling all but the most difficult controlled elements, the dual-loop model indicates that the necessity of lead equalization in the form of error rate utilization is obviated. Likewise, apparent error lag equalization for pure gain controlled elements is accomplished by inner-loop activity.

Further research appears warranted along the following lines:

1. Application of the dual-loop model to multi-axis tracking tasks should be investigated.

2. Synthesis techniques should be sought which would allow the selection of model parameter values in the absence of experimental data, given the characteristics of disturbances, controlled elements, displays, and manipulators.

3. The selection of appropriate internal models of manipulator-controlled element dynamics should receive more attention. From the modeling results with $K/(s^3 + 12.3s^2 + 11.6s)$ and $K/(s - 2)$ controlled element dynamics, it appears that simplified internal models accurate in the region beyond crossover are sufficient and appropriate.

4. More detailed modeling of the hypothesized threshold and switching logic of the nonlinear form of the dual-loop model should be undertaken.

5. Finally, the use of the dual-loop model structure to study human controller learning behavior should be pursued.

REFERENCES

1. McRuer, D. T.; Graham, D.; Krendel, E.; and Reisener, W. Jr.: Human Pilot Dynamics in Compensatory Systems. AFFDL-TR-65-15, Air Force Flight Dynamics Laboratory, 1965.

2. Gordon-Smith, M.: An Investigation into Certain Aspects of the Describing Function of a Human Operator Controlling a System of One Degree of Freedom. Proceedings of the Fifth Annual Conference on Manual Control, March 1969, pp. 203-242.

3. Stapleford, R. L; McRuer, D. T.; and Magdaleno, R.: Pilot Describing Function Measurements in a Multiloop Task. NASA CR-542, 1966.

4. Smith, R. H.: A Unified Theory for Pilot Opinion Rating. Proceedings of the Twelfth Annual Conference on Manual Control, May 1976, pp. 542-558.

5. Magdaleno, R. E.; and McRuer, D. T.: Experimental Validation and Analytical Elaboration for Models of the Pilot's Neuromuscular Sub-System in Tracking Tasks. NASA CR-1757, 1971.

6. Kleinman, D. L.; Baron, S.; and Levison, W. H.: An Optimal Control Model of Human Response, Part I. Automatica, vol. 6, 1970, pp. 357-369.

7. Levison, W. H.; Baron, S.; and Junker, A. M.: Modeling the Effects of Environmental Factors on Human Control and Information Processing. AMRL-TR-76-74, Aerospace Medical Research Laboratory, 1976.

8. Levison, W. H.; Elkind, J. I.; and Ward, J. L.: Studies of Multivariable Manual Control Systems: A Model for Task Interference. NASA CR-1746, 1971.

9. Levison, W. H.; Baron, S.; and Kleinman, D. L.: A Model for Human Controller Remnant. IEEE Transactions on Man-Machine Systems, vol. MMS-10, no. 4, 1969, pp. 101-108.

10. Wewerinke, P. H.: Human Operator Workload for Various Control Situations. Proceedings of the Tenth Annual Conference on Manual Control, April 1974, pp. 167-192.

11. Jex, H. R.; Allen, R. W.; and Magdaleno, R. E.: Display Format Effects on Precision Tracking Performance, Describing Functions, and Remnant. AMRL-TR-71-63, Aerospace Medical Research Laboratory, 1971.

12. Hess, R. A.; and Teichgraber, W. M.: Error Quantization Effects in Compensatory Tracking Tasks. IEEE Transactions on Systems, Man and Cybernetics, vol. SMC-4, no. 4, 1974, pp. 343-349.

13. Jex, H. R.; and Allen, R. W.: Research on a New Human Dynamic Response Test Battery. Proceedings of the Sixth Annual Conference on Manual Control, April 1970, pp. 743-777.

14. McRuer, D. T.; Hofmann, L. G.; Jex, H. R.; Moore, G. P.; Phatak, A. V.; Weir, D. H.; and Wolkovitch, J.: New Approaches to Human-Pilot/Vehicle Dynamic Analysis. AFFDL-TR-67-150, Air Force Flight Dynamics Laboratory, 1968.

15. McDonnell, J. D.; and Jex, H. R.: A "Critical" Tracking Task for Man-Machine Research Related to the Operator's Effective Time Delay, Part II. NASA CR-674, 1967.

TABLE 1.- DUAL-LOOP MODEL PARAMETERS

Expression	Description
$Y_{p_e} = \frac{K_e(T_L s + 1)}{(T_e s + 1)^a}$	displayed error equalization, $a = 1, 2, \ldots$
$Y_{p_{\dot{m}}} = \frac{K_{\dot{m}} s^b}{(T_m s + 1)^b}$	control rate equalization, $b = 1, 2, \ldots$
$Y_{\delta}\hat{Y}_c$	human controller's internal model of manipulator-controlled element dynamics
$Y_{p_n} = \frac{1}{\left(\frac{s}{\omega_n}\right)^2 + \frac{2\zeta_n}{\omega_n} s + 1}$	neuromuscular dynamics
r_e	remnant injected into displayed error
$r_{\dot{u}}$	remnant injected into inner loop
$Y_p = \frac{u_\delta}{e_d} = \frac{Y_{p_e} Y_{p_n}}{1 + Y_{p_n} Y_\delta \hat{Y}_c Y_{p_{\dot{m}}} s}$	equivalent single-loop human controller describing function.

TABLE 2.- SUMMARY OF DUAL-LOOP MODELING RESULTS

$Y_\delta Y_c$	$Y_\delta \hat{Y}_c$	K_e	T_L, sec	K_m, sec	T_m, sec	τ, sec	ζ_n	ω_n, rad/sec
1.0	1.0	2.5	0	0.5	1.0	0.1	0.1	20
1/s	1/s	18.0	0	6.0	2.0	.13	.3	15
$1/s^2$	$1/s^2$	26.5	0	32.3	3.33	.16	.7	15
$145/\Delta$[a]	$10/s^2$	1.4	0	1.0	1.25	.19	.7	15
$2.82/s(s-1)$[b]	$2.82/s(s-1)$	5.5	0.33	10.0	3.33	.15	.1	15
$1/s)_p$[c]	1/s	5.6	0	10.0	20.0	.13	.5	20

[a] $\Delta = s^3 + 12.3s^2 + 11.6s$.

[b] Higher-order controller model used.

[c] Peripheral display used.

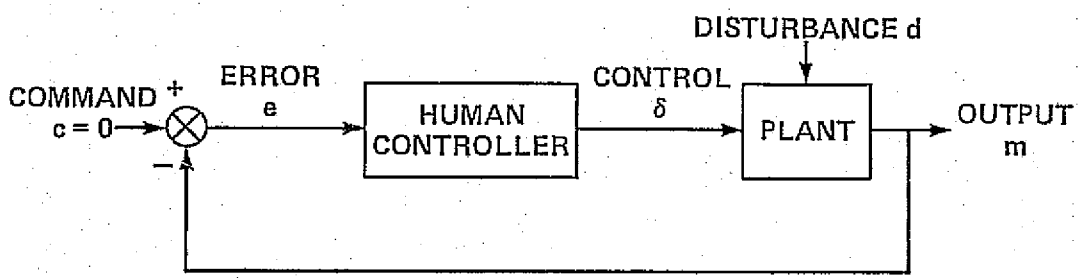

Figure 1.- Single-axis compensatory tracking task.

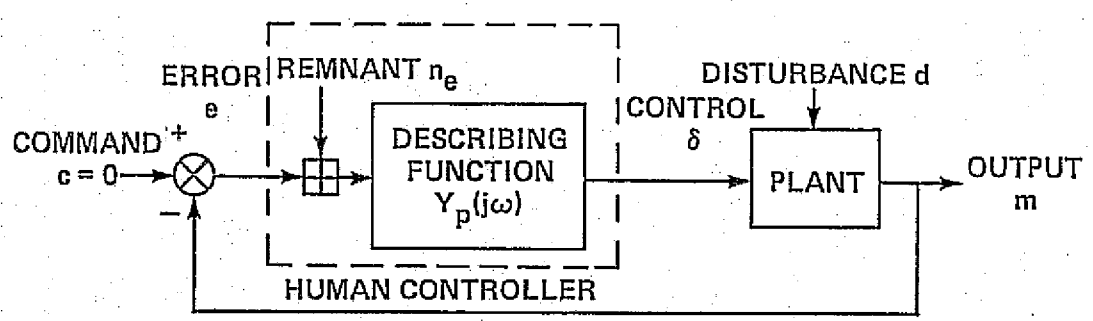

Figure 2.- Quasi-linear model of the human controller in a single-axis compensatory tracking task.

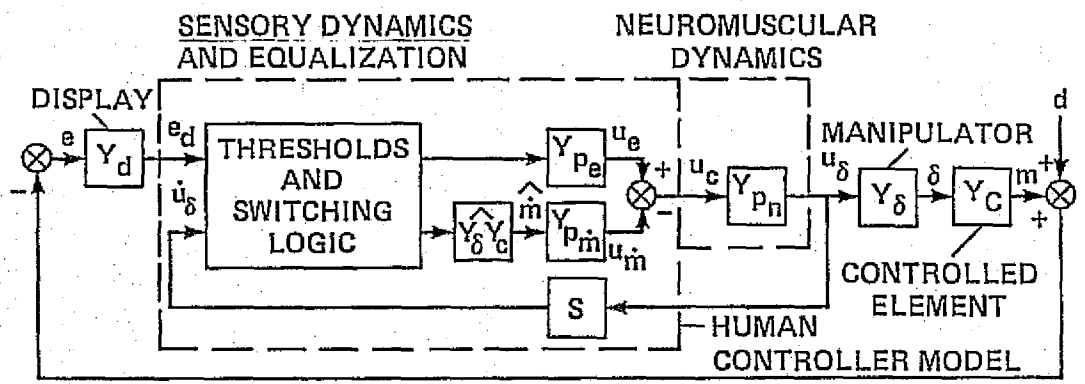

Figure 3.- Nonlinear dual-loop model of the human controller in a single-axis compensatory tracking task.

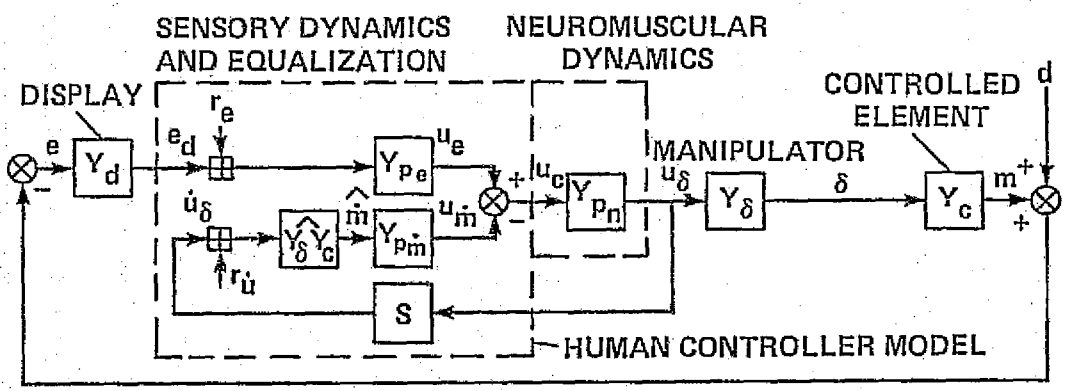

Figure 4.- Quasi-linear dual-loop model of the human controller in a single-axis compensatory tracking task.

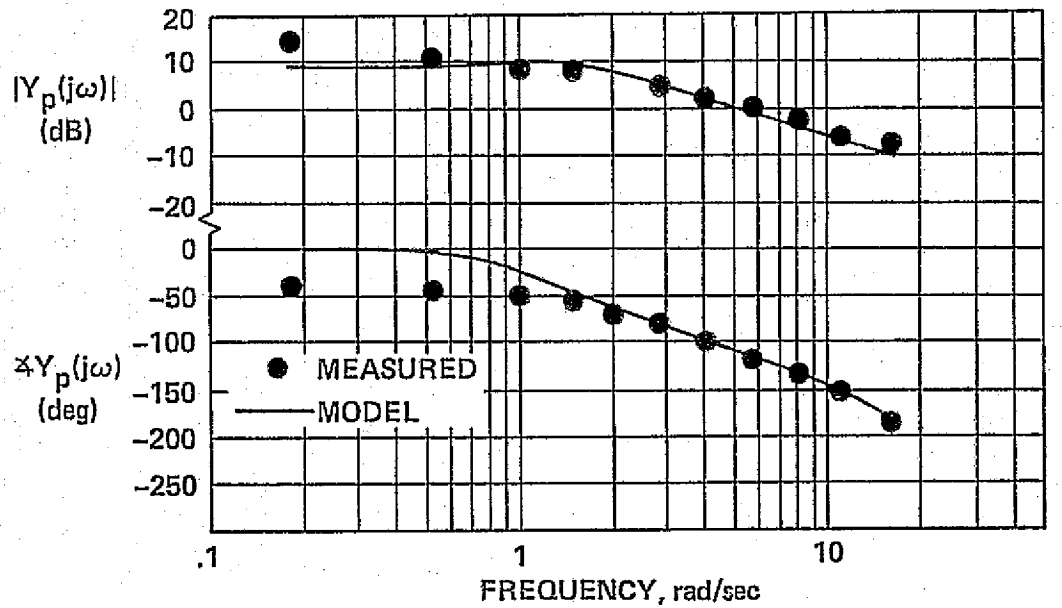

Figure 5.- Comparison between measured and dual-loop model describing functions for K dynamics.

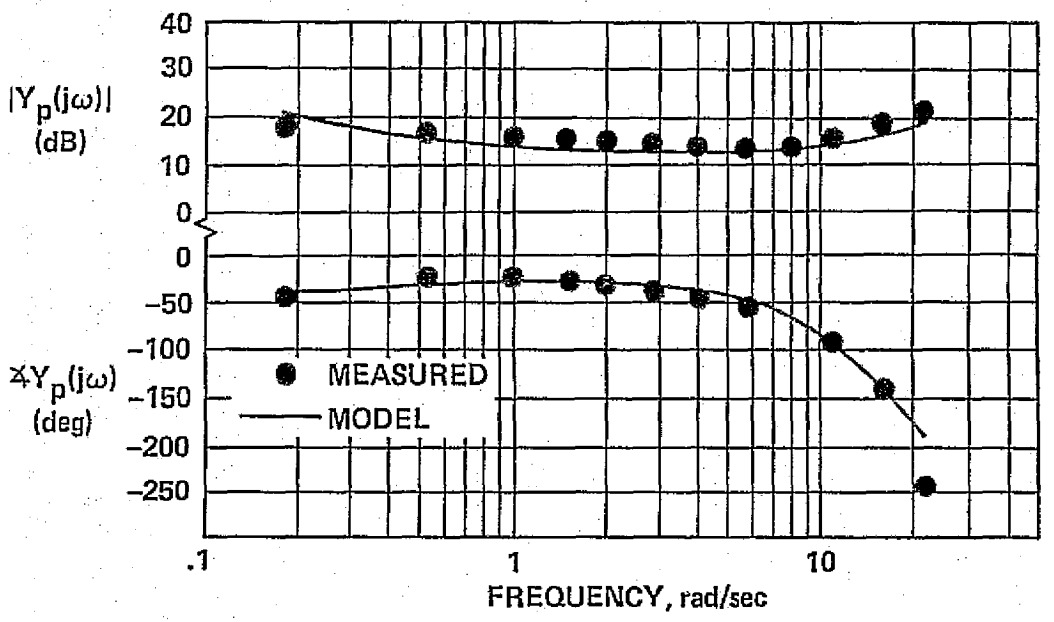

Figure 6.- Comparison between measured and dual-loop model describing functions for K/s dynamics.

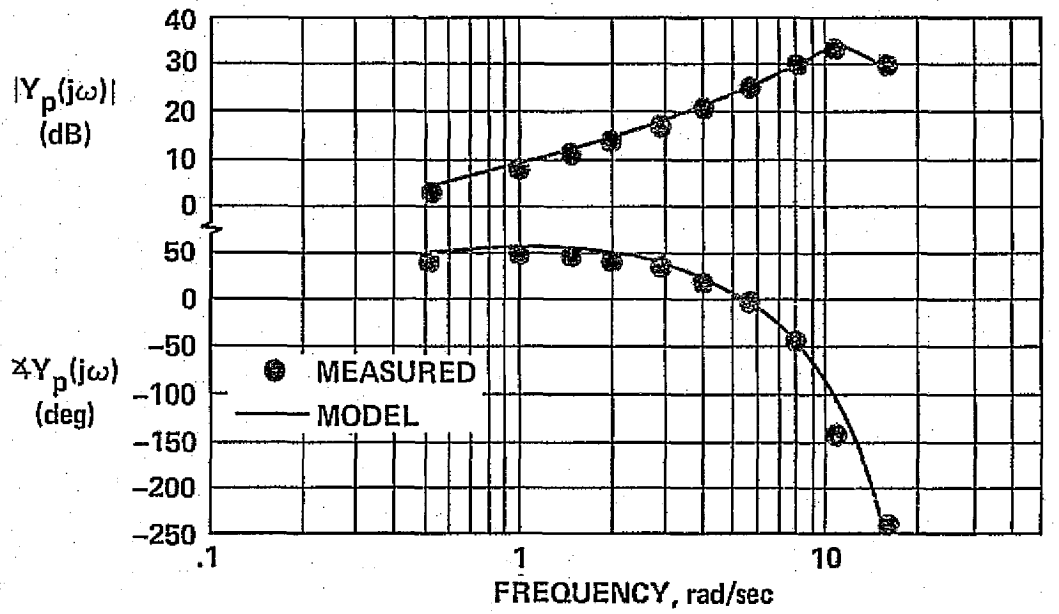

Figure 7.- Comparison between measured and dual-loop model describing functions for K/s^2 dynamics.

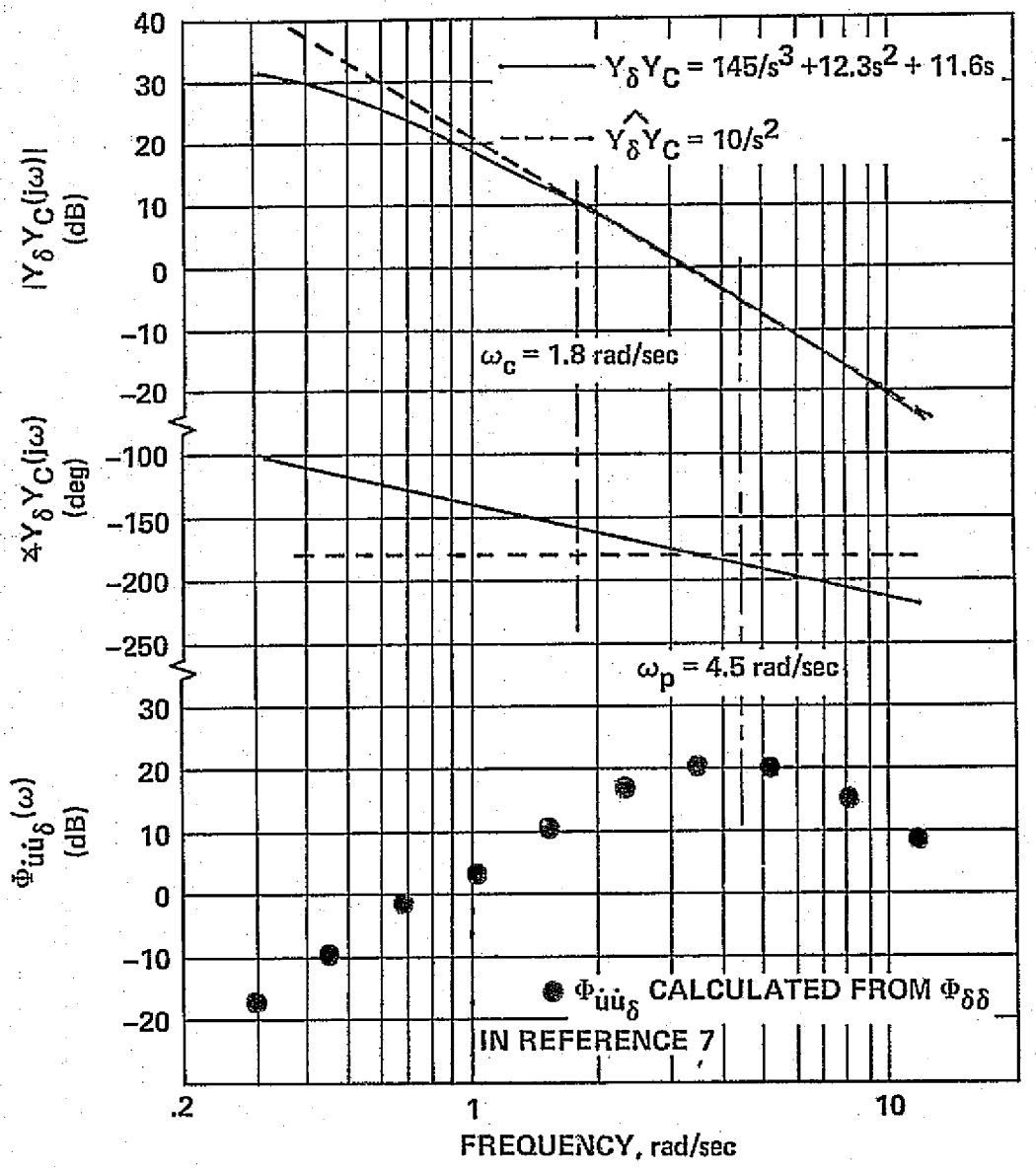

Figure 8.- Approximate and exact manipulator-controlled element dynamics and correlated control rate spectrum for $K/(s^3 + 12.3s^2 + 11.6s)$ dynamics.

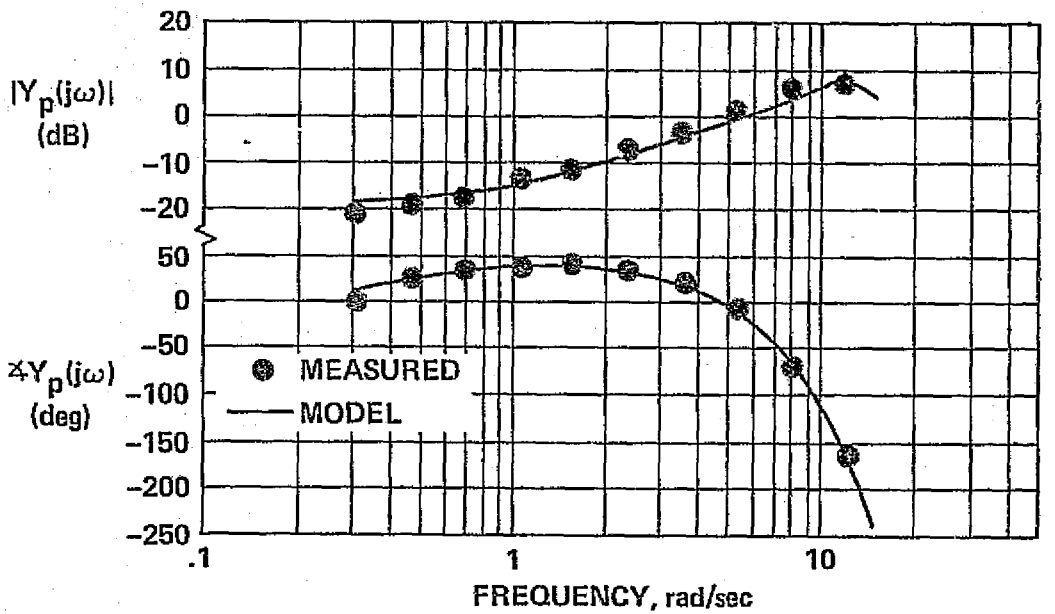

Figure 9.- Comparison between measured and dual-loop model describing functions for $K/(s^3 + 12.3s^2 + 11.6s)$ dynamics.

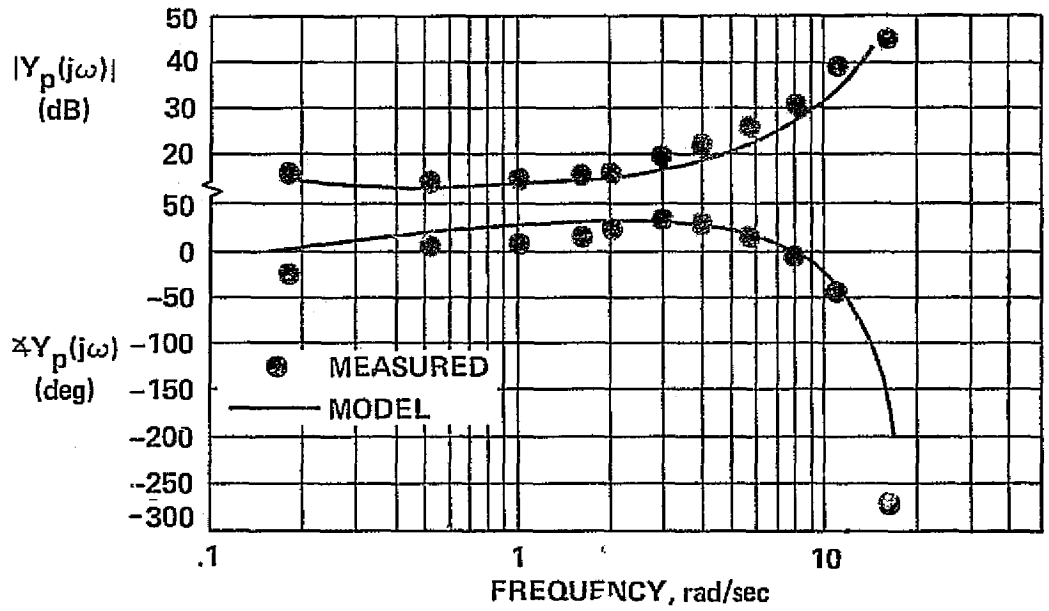

Figure 10.- Comparison between measured and dual-loop model describing functions for K/s(s - 1) dynamics.

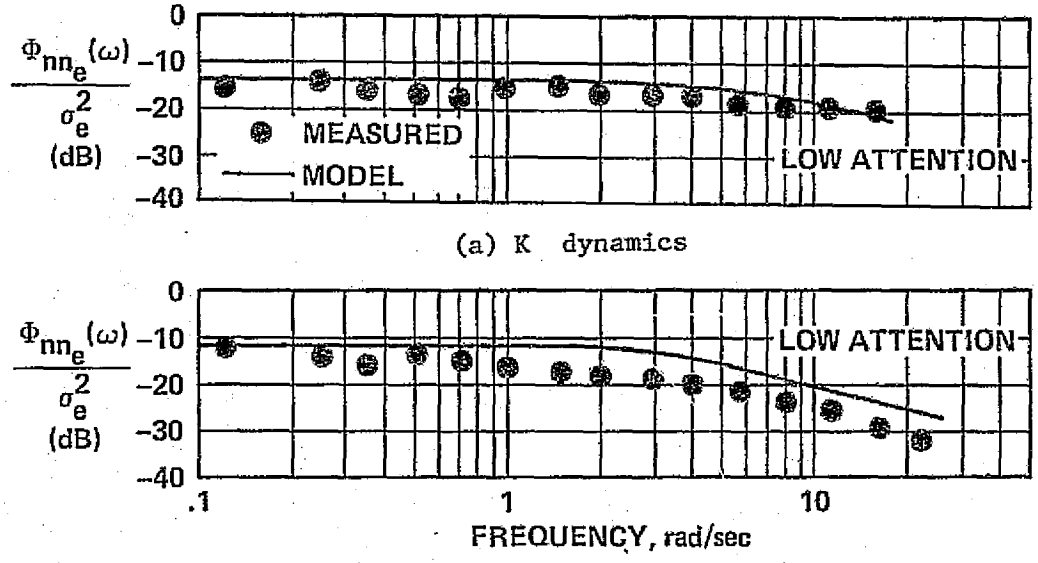

(a) K dynamics

(b) K/s dynamics

Figure 11.- Comparison between measured and empirical injected remnant spectra for K dynamics; for K/s dynamics; for K/s^2 dynamics; and for K/s(s - 1) dynamics.

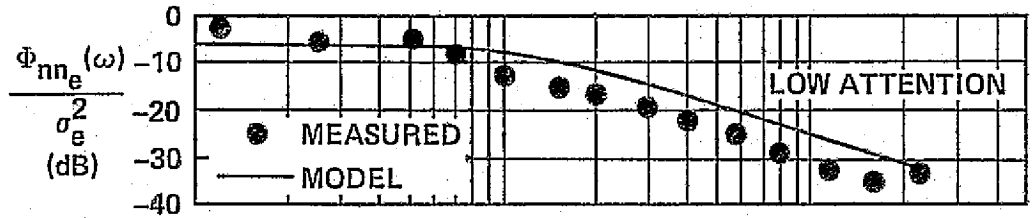

(c) K/s^2 dynamics.

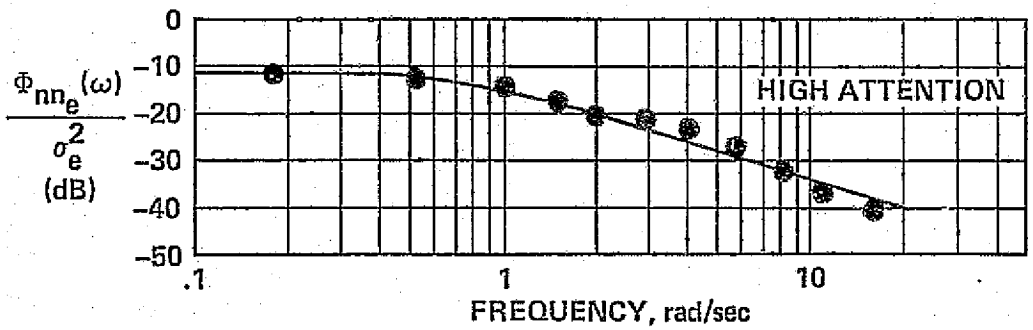

(d) $K/s(s - 1)$ dynamics

Figure 11.- Concluded.

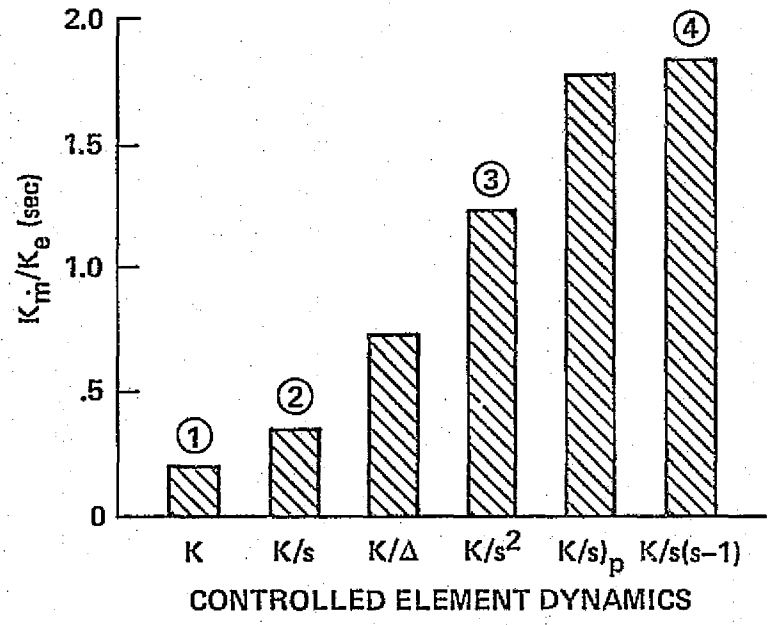

$\Delta = s^3 + 12.3s^2 + 11.6s$

$K/s)_p$ DENOTES 22° PERIPHERAL VIEWING

ⓝ "DEGREE OF EFFORT" EXPENDED IN CONTROLLING K, K/s, K/s^2 AND K/s(s–1) DYNAMICS AS DOCUMENTED IN REFERENCE 10,

① = LEAST EFFORT

Figure 12.- $K_m^{\cdot}/K_e$ for various controlled element dynamics.

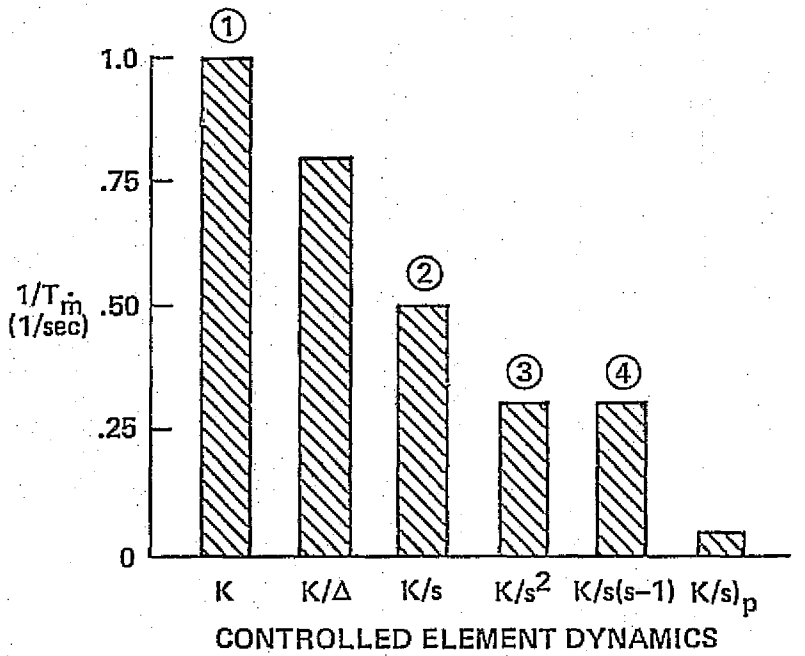

$\Delta = s^3 + 12.3s^2 + 11.6s$

$K/s)_p$ DENOTES 22° PERIPHERAL VIEWING

ⓝ "DEGREE OF EFFORT" EXPENDED IN CONTROLLING K, K/s, K/s^2 AND K/s(s–1) DYNAMICS AS DOCUMENTED IN REFERENCE 10,
① = LEAST EFFORT

Figure 13.- $1/T_{\dot{m}}$ for various controlled element dynamics.

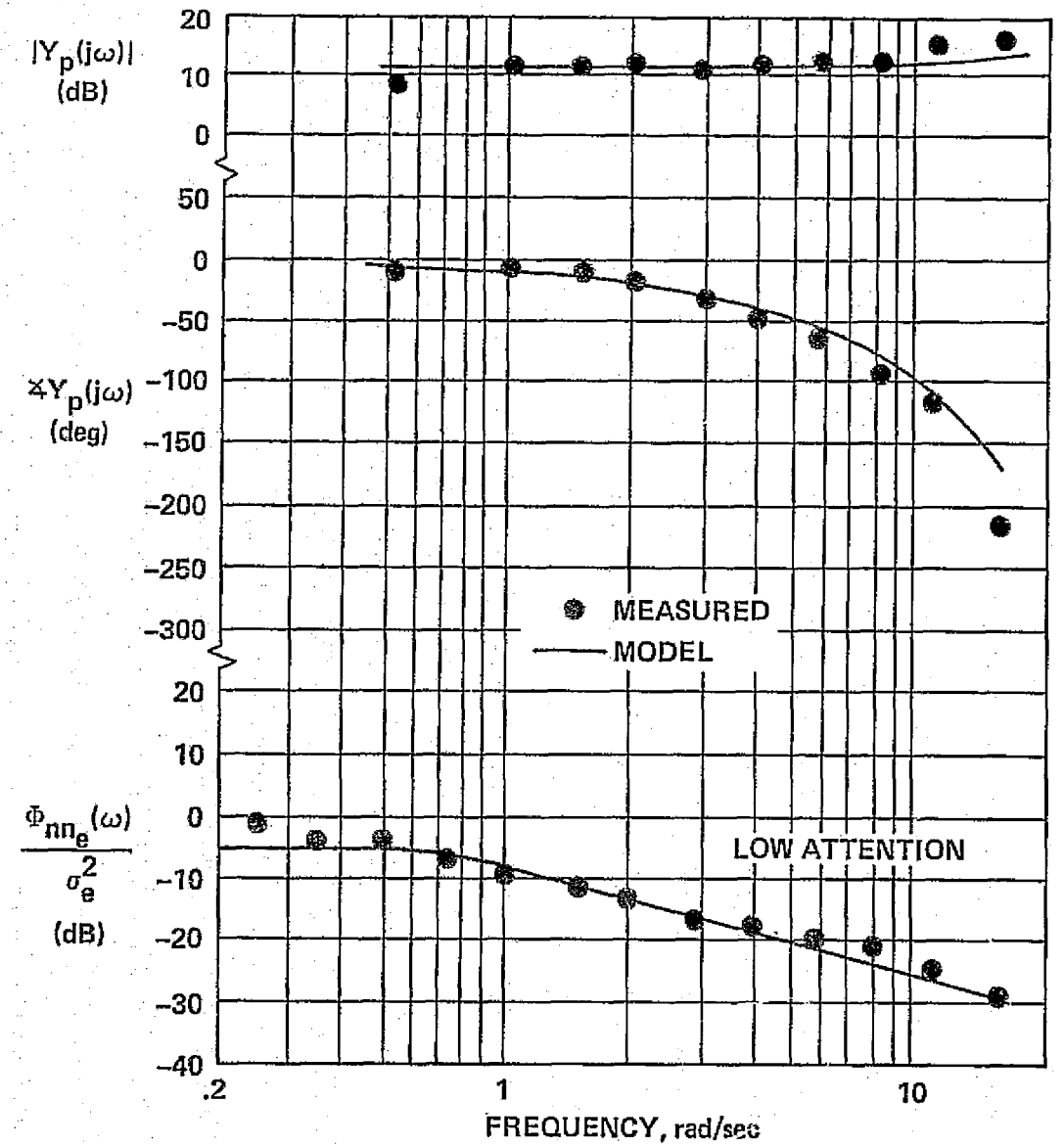

Figure 14.- Comparison between measured and dual-loop describing functions and injected remnant spectra for K/s dynamics and 22° peripheral viewing.

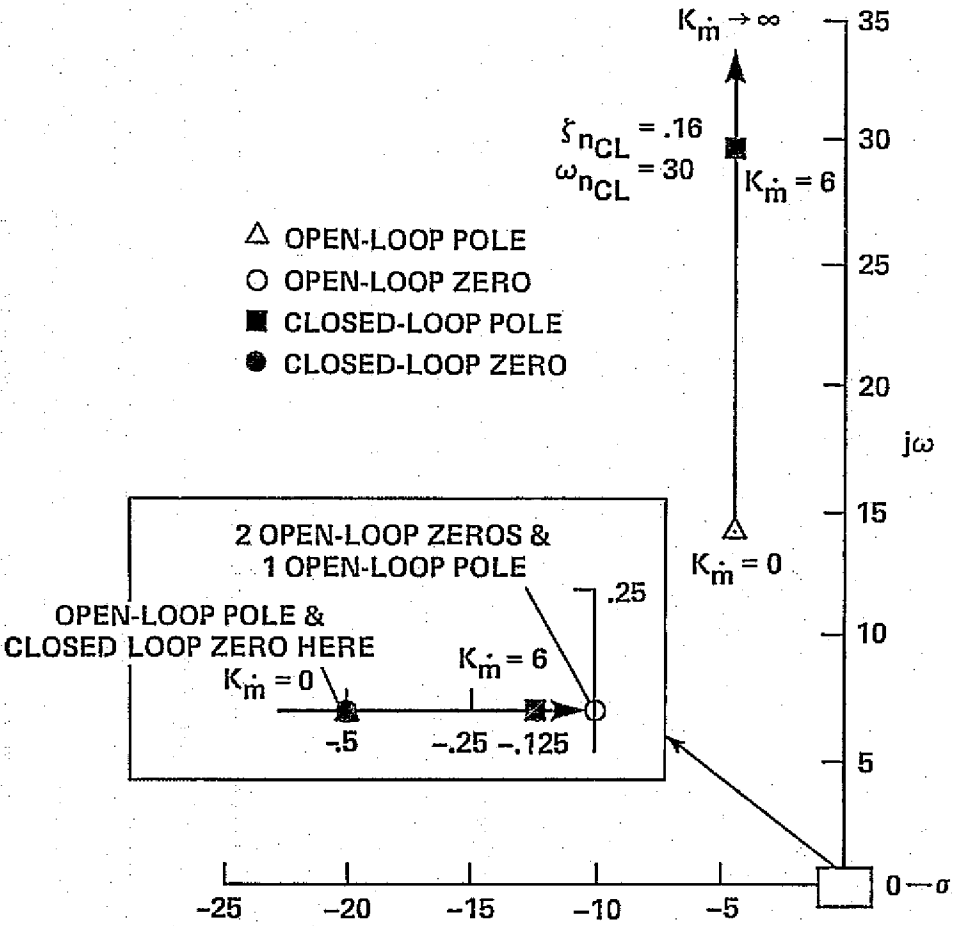

Figure 15.- Closed-loop poles and zeros of δ/u_e inner-loop human controller describing function as a function of $K_{\dot{m}}$; K/s controlled element dynamics, foveal viewing.

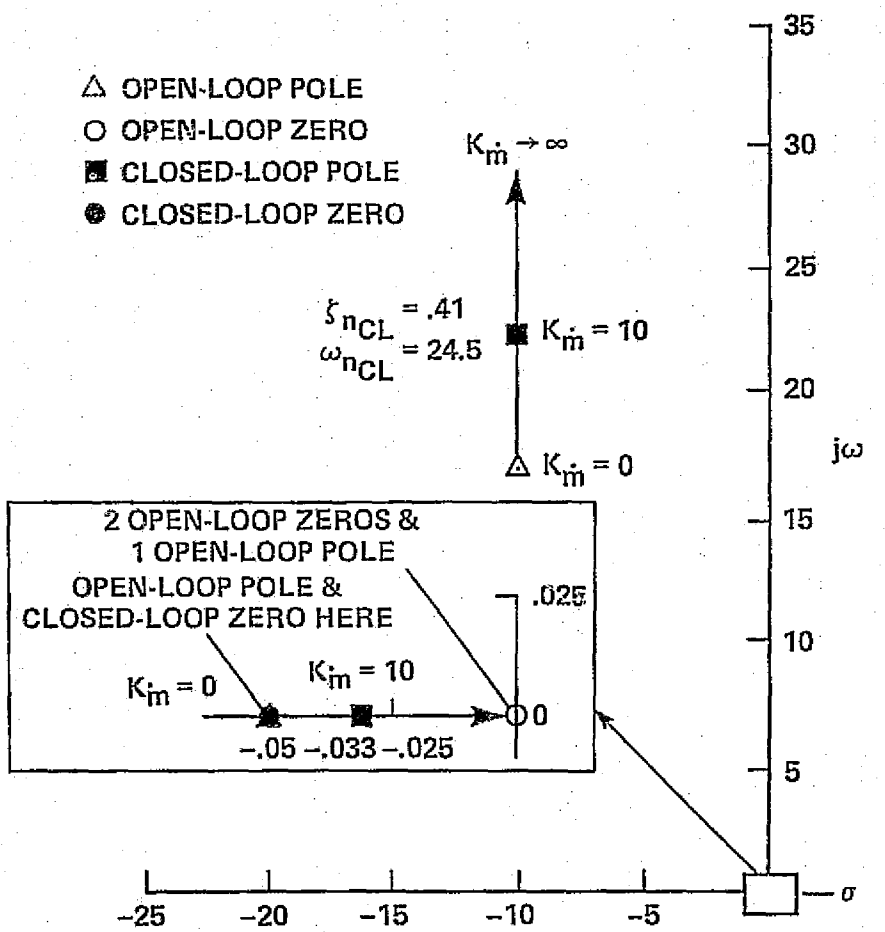

Figure 16.- Closed-loop poles and zeros of δ/u_e inner-loop human controller describing function as a function of $K_{\dot{m}}$; K/s controlled element dynamics, 22° peripheral viewing.

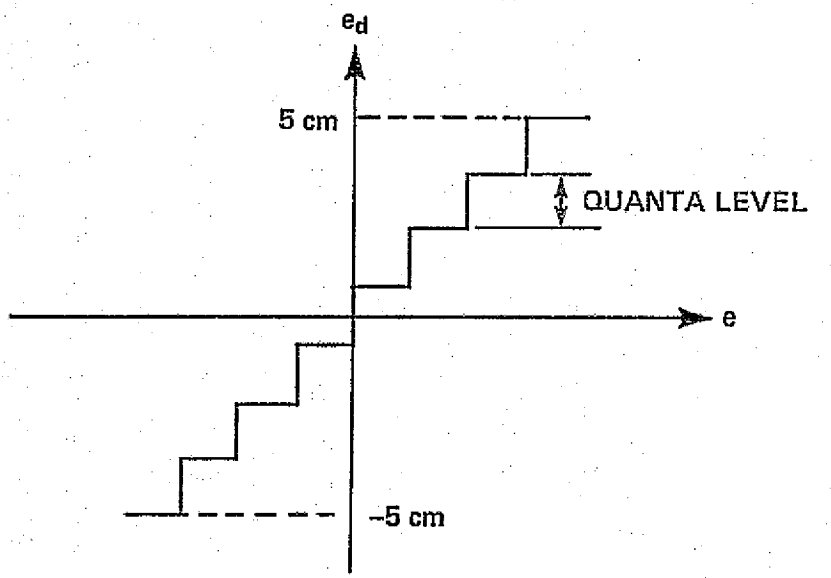

QUANTA LEVELS
(cm)

0 (CONTINUOUS)	.7257
.0635	1.0160
.2540	1.2700
.5080	1.6933

Figure 17.- Quantization format for experiment of reference 12.

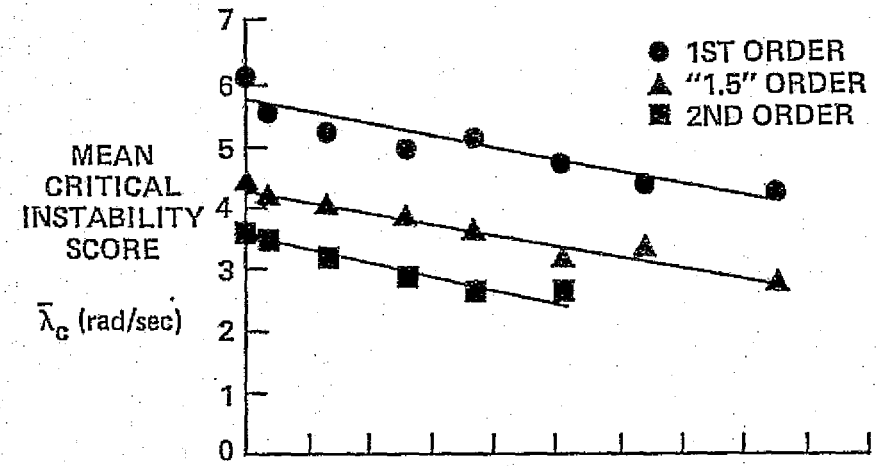

Figure 18.- Critical instability scores for quantized display (subject A).

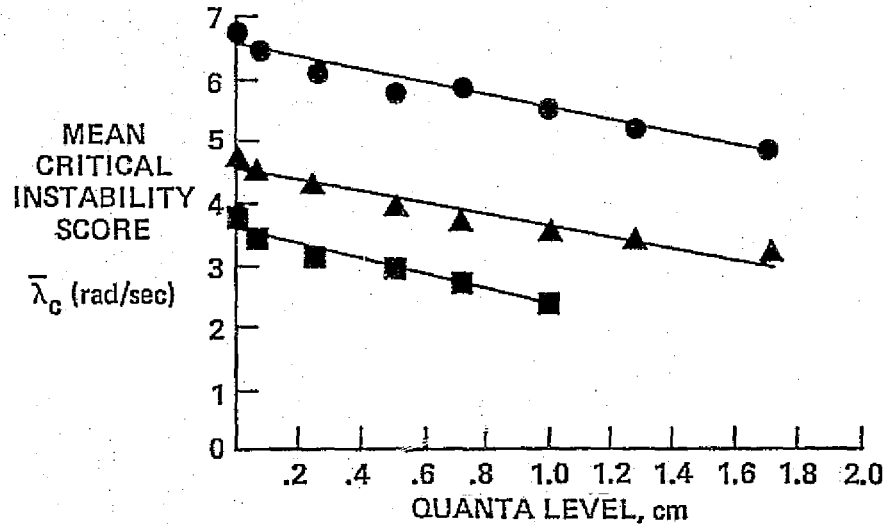

Figure 19.- Critical instability scores for quantized display (subject B).

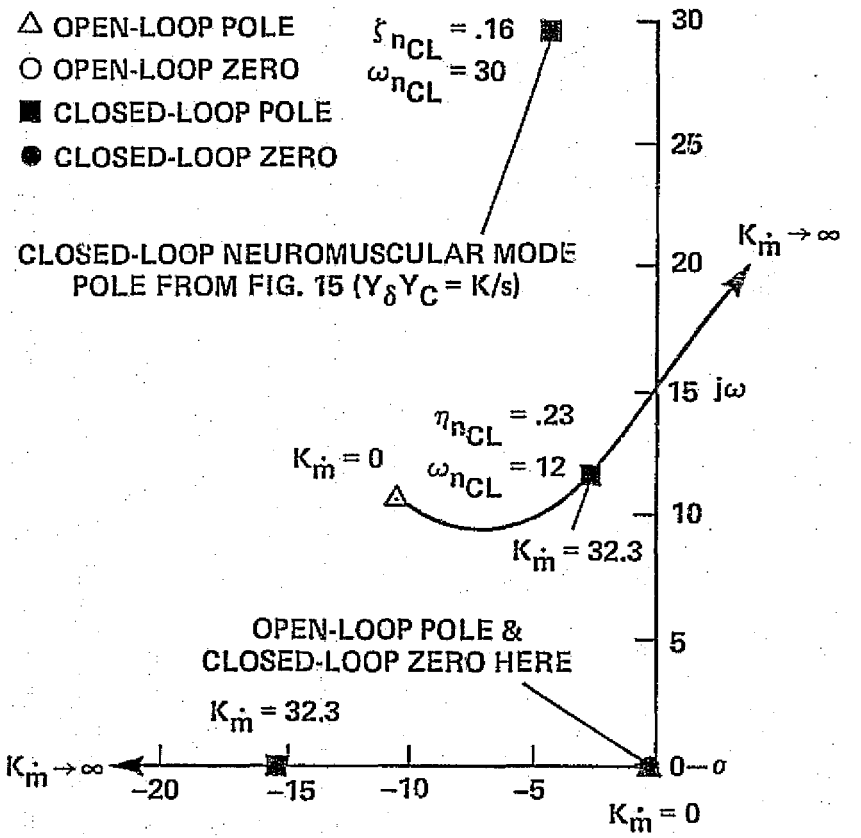

Figure 20.- Closed-loop poles and zeros of δ/u_e inner-loop human controller describing function as a function of $K_{\dot{m}}$; K/s^2 controlled element dynamics.

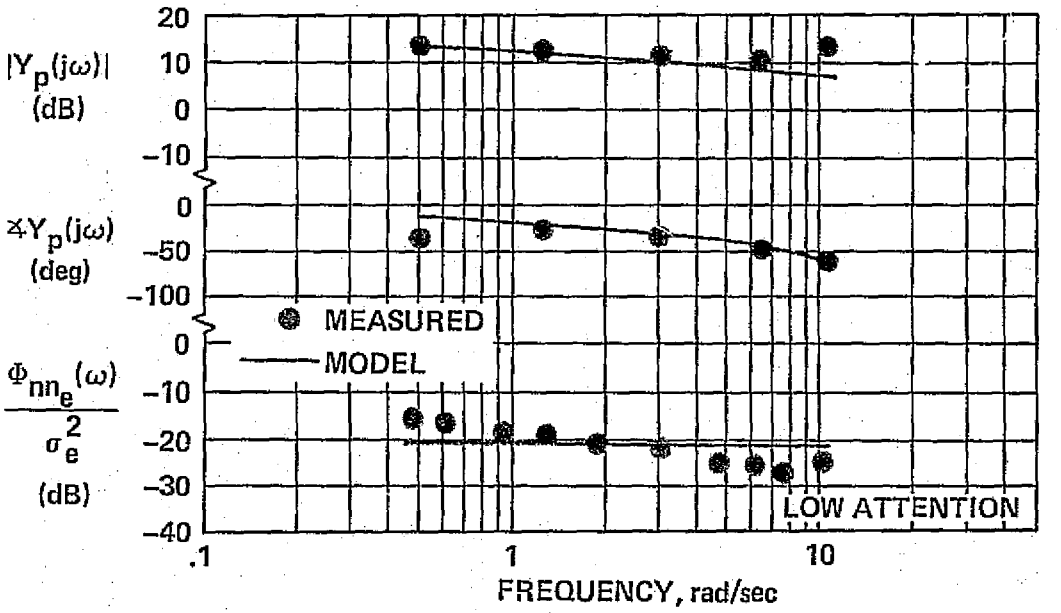

Figure 21.- Comparison between measured and dual-loop describing functions and injected remnant spectra for $K/(s - 2)$ dynamics.

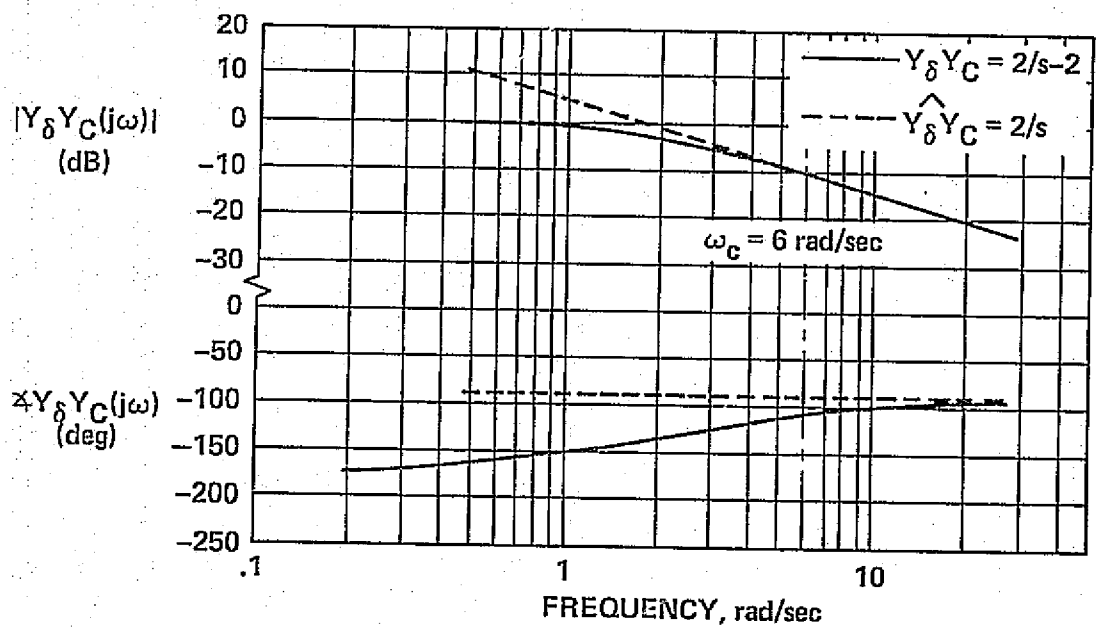

Figure 22.- Approximate and exact manipulator-controlled element dynamics for $K/(s - 2)$ dynamics.

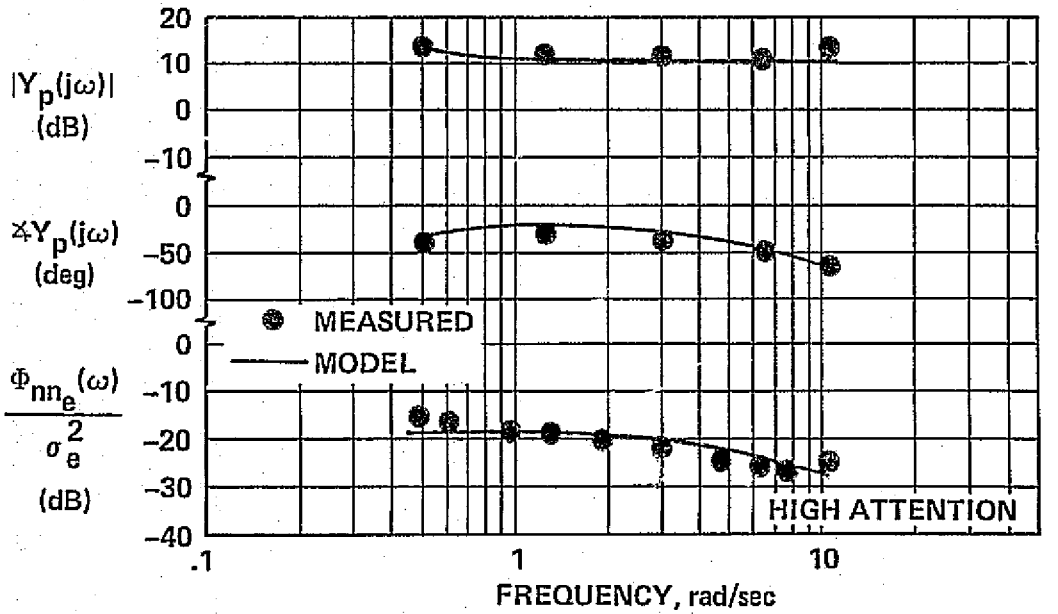

Figure 23.- Comparison between measured and dual-loop model describing functions and injected remnant spectra for K/(s - 2) dynamics; simplified internal model.

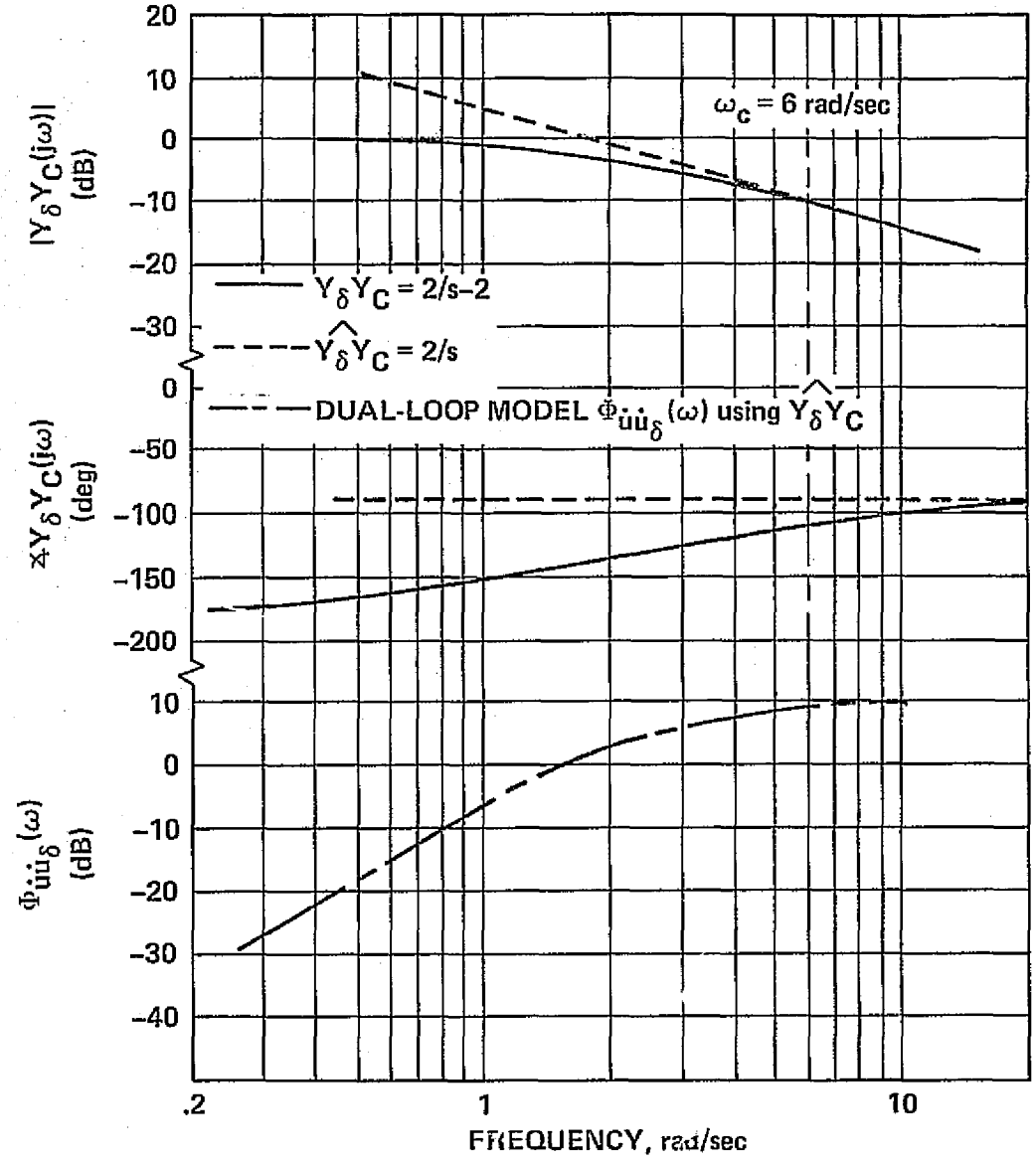

Figure 24.- Approximate and exact manipulator-controlled element dynamics and dual-loop model correlated control rate spectrum for K/(s - 2) dynamics.

1. Report No. NASA TM-73,249	2. Government Accession No.	3. Recipient's Catalog No.
4. Title and Subtitle A DUAL-LOOP MODEL OF THE HUMAN CONTROLLER IN SINGLE-AXIS TRACKING TASKS		5. Report Date 6. Performing Organization Code
7. Author(s) Ronald A. Hess		8. Performing Organization Report No. A-7064
9. Performing Organization Name and Address Ames Research Center Moffett Field, Calif. 94035		10. Work Unit No. 513-54-01 11. Contract or Grant No.
12. Sponsoring Agency Name and Address National Aeronautics and Space Administration Washington, D.C. 20546		13. Type of Report and Period Covered Technical Memorandum 14. Sponsoring Agency Code

15. Supplementary Notes

16. Abstract

A dual-loop model of the human controller in single-axis compensatory tracking tasks is introduced. This model possesses an inner-loop closure which involves feeding back that portion of controlled element output rate which is due to control activity. The sensory inputs to the human controller are assumed to be system error and control force. The former is assumed to be sensed via visual, aural, or tactile displays while the latter is assumed to be sensed in kinesthetic fashion. A nonlinear form of the model is briefly discussed. This model is then linearized and parameterized. A set of general adaptive characteristics for the parameterized model is hypothesized. These characteristics describe the manner in which the parameters in the linearized model will vary with such things as display quality. It is demonstrated that the parameterized model can produce controller describing functions which closely approximate those measured in laboratory tracking tasks for a wide variety of controlled elements. The explicit consideration of the inner-loop closure in the model allows much of the adaptive nature of the human controller to be explained in a systematic manner. In this respect, the dual-loop model is superior to existing single-loop structures. An empirically derived expression for the normalized injected error remnant spectrum is introduced. The expression utilizes a pair of dual-loop model parameters. Finally, using the dual-loop model, the effects of some specific display and manipulator variations on controller describing functions, remnant spectra, and critical tracking task scores are explained.

17. Key Words (Suggested by Author(s))	18. Distribution Statement
Pilot models Compensatory tracking	Unlimited STAR Category - 08

19. Security Classif. (of this report)	20. Security Classif. (of this page)	21. No. of Pages	22. Price*
Unclassified	Unclassified	57	$4.25

*For sale by the National Technical Information Service, Springfield, Virginia 22161